Worcester Polytechnic Institute
Major Qualifying Project Report

USER STUDY AND OPTIMIZATION OF WEARABLE TRANSCUTANEOUS OXYGEN SENSOR

April 27, 2023

Undergraduate Students

Sydney Hobson

Biomedical Engineering

sahobson@wpi.edu

Abigail Leonardi

Electrical and Computer Engineering

awleonardi@wpi.edu

Ciara Murphy

Biomedical Engineering

cmurphy@wpi.edu

Vanshika Rohera

Electrical and Computer Engineering

vrohera@wpi.edu

Advisor

Professor Ulkuhan Guler

uguler@wpi.edu

Contents

Abstract

Respiratory illnesses continue to be a significant concern in the medical field, and their prevalence has only grown since the coronavirus disease of 2019 (COVID-19) pandemic. As a result, there is a need for reliable medical devices for remote monitoring. The existing technology presents limitations which do not allow for patient autonomy where the individual can be continuously monitored from their home. The technology in development has the potential to mitigate these shortcomings. The aim of this user study is to verify the accuracy of a wearable transcutaneous oxygen sensor and optimize its design and processing capabilities. In order to assess the viability of a current transcutaneous oxygen sensor prototype, a laboratory-based small human subject test was conducted to validate the sensor and characterize its performance. Qualitative research was conducted to improve the data processing methods as well as user comfort through wearability.

Executive Summary

Respiratory illnesses factor into leading causes of death worldwide. Accurate oxygen monitoring is crucial and can help mitigate respiratory illnesses by allowing for real-time tracking of patients. Following the COVID-19 pandemic in 2020, the need for respiratory monitoring and remote care became a primary concern worldwide. The need for remote monitoring has continued to grow. Technological developments allow for patients to be monitored accurately and consistently without needing to be tethered to machines. These advancements allow for increased patient comfort and absolve dignity concerns in times of fatal health conditions and hospice.

Recent developments in the field of respiratory monitoring include a transcutaneous oxygen sensor. The device being analyzed in this report is unique because it uses an oxygen-quenching film to take measurements. The gold standard in the industry is pulse oximetry (PPG) which reflects light off the skin to gather measurements. However, this technique does have disadvantages. Most alarmingly, noted discrepancies when measuring blood oxygen in people of color. Due to different absorption rates of light based on the skin's pigment, the readings can become less accurate based on the biological makeup of the subject. This creates concerns for people of color in relation to accurate monitoring of their respiratory functions. Measuring the oxygen quenching film instead of the skin has the potential to reduce inaccuracies as skin pigment should not factor into the sensor measurement process.

The device is currently in the development stage and has a working prototype. However, further testing needed to be conducted to ensure the medical grade potential of the device. To verify if the prototype would be usable in the medical industry, the sensor must report consistent and accurate measurements across a wide range of patients. Thus, extensive testing was conducted on four participants utilizing the sensor on various body locations. The purpose of the testing was as follows.

1. Standardize a procedure to take measurements;
2. Observe potential errors and points of improvement;
3. Verify consistency and repeatability of readings;
4. Determine optimal location for potential remote monitoring application;
5. Improve user comfort through wearability.

Following the conclusion of human subject testing, the data was further analyzed, and the PCB sensor design was modified for user comfort. The testing indicated

the technology was capable of producing accurate and repeatable measurements. However, outliers during data collection often arose because of the lack of proper sensor encapsulation. An example of an error caused by a lack of encapsulation is the rush of oxygen which occurs when a subject moves slightly and the sensing film is exposed to ambient air. Therefore, experimentation in data processing was conducted to assess how different MATLAB functions impacted the data. Specifically, the functions tested in MATLAB included the Hampel, rmoutliers, filloutliers, and moving average filters. After processing data with outliers, the team concluded that the Hampel filter yielded the best results while maintaining the integrity of the data.

To help adapt the technology to future use in remote monitoring, the PCB needs to be miniaturized to promote user comfort through wearability. Ideally, a product produced for remote patient monitoring should be small enough not to compromise the user's quality of life during the testing period. Human subject tests were performed with a prototype built on a rigid PCB. However, as test verification has proved the sensor's functionality, the next stage of board design is user-centric. Ease of wearability and comfort are two concerns that are addressed through re-sizing the PCB. In order to reduce the overall size of the prototype, a rigid-flex PCB could be used to create a foldable design. This design exhibits the benefits of shrinking the overall size of the PCB while maintaining an equivalent surface area. Therefore, the components and layout verified in testing are directly transferable to the modified PCB. By reducing the area of the PCB, the design can be easily encapsulated into a wearable device for users to keep on throughout the day.

While verification of the sensor's capabilities has been successful, there are a number of future modifications which can be implemented. The modifications will retain the core technology while allowing for an easier transition to a product suitable for remote patient monitoring. Ultimately, this Major Qualifying Project (MQP) helped verify the proficiency of an existing transcutaneous oxygen sensor prototype developed at Worcester Polytechnic Institute's (WPI) Integrated Circuits and System Lab (ICAS Lab) and recommended measurement sites on the body as well as made recommendations for future developments.

0.1 Contributions

During the project, the team wrote two conference papers. The first paper was submitted and accepted to the IEEE Engineering in Medicine and Biology Conference. It focuses on a user study to determine the optimal location on the human body to conduct $PtcO_2$ measurements. All locations consistently reported accurate and reliable data. Among them, the thumb demonstrated shorter settling times and the

most uniform luminescence lifetime values [1]. The second paper will be submitted to the MIT Undergraduate Research Technology Conference. It focuses on outlier detection and removal for the $PtcO_2$ sensor. The goal of signal processing is to remove prominent outliers and smooth deviations in the data without losing the integrity of the initial signal. The Hampel filter in MATLAB was the most successful at detecting outliers, and the fillmissing function with the previous or linear interpolation method was the most successful at replacing outliers [2].

List of Figures

List of Tables

1 Introduction

1.1 Motivations

1.1.1 Importance of Monitoring Respiration Parameters

Respiration is crucial to the survival of the human body. Respiration ensures cellular gas exchange, acid-base regulation, and overall homeostasis [9]. Respiratory rate is an indicator of patient health deterioration and aids in disease diagnosis [10]. Moreover, the respiratory rate varies in response to stressors such as emotional stress and temperature [10]. Monitoring respiration is important as respiratory diseases impact millions worldwide [11]. Two of the top five leading causes of death are respiratory illnesses: chronic obtrusive pulmonary disease (COPD) and lower respiratory disease [12].

1.1.2 Relevance to COVID-19

As the world evolves, the need for accurate bedside and remote respiratory medical devices persists. The COVID-1) pandemic exacerbated these issues, contributing to over 6.8 million deaths [11]. The virus itself, SARS-CoV-2, infects cells along the respiration airways of the lungs. By attaching to the ACE-2 receptor on a healthy cell, the virus can infect this cell by reproducing [13]. These strains then continue to affect other surrounding cells, causing the human to have symptoms of COVID-19 such as shortness of breath and even respiratory failure [14]. In severe cases, some patients may need to use a ventilator to assist their breathing [15]. Monitoring respiration can help detect early signs of respiratory decline and therefore help medical professionals determine more effective and accurate treatment options.

1.1.3 What is Transcutaneous Oxygen?

The circulatory system is responsible for delivering oxygen to tissues within the body. Blood is oxygenated in the lungs and then circulated around the body through the arteries [16]. Microcirculation is responsible for oxygen delivery from the red blood cells to the tissues [17]. Since blood gas parameters can indicate a patient's respiratory status, it is important to measure blood oxygen. The most accurate method to measure blood oxygen is through using an arterial blood gas test [18]. However, this method is invasive and does not provide instant data [19]. Noninvasive, surrogate contact methods of measuring blood oxygen has become increasingly popular as they are still accurate at detecting blood oxygen levels. Transcutaneous oxygen

specifically measures the partial pressure of oxygen from blood immediately below the skin [20].

1.1.4 Difference Between Transcutaneous Oxygen Monitoring and Pulse Oximetry

Pulse oximetry is a measure of blood oxygen saturation (SpO_2) and transcutaneous oxygen is the measure of the partial pressure of oxygen on the skin surface ($PtcO_2$). Both methods provide insight into the levels of oxygen in the blood. Pulse oximetry utilizes specific wavelengths of light and their corresponding absorbance rate when shined on the skin [21]. Oxygenated hemoglobin and de-oxygenated hemoglobin absorb different wavelengths of light [21]. Oxygenated hemoglobin absorbs more infrared light than deoxygenated hemoglobin, and deoxygenated hemoglobin absorbs more red light than oxygenated hemoglobin [22]. An LED is shined onto the skin and the absorbance is quantified by the photodiode on the opposite side of the LED. Using this information, blood oxygenation saturation can be calculated based on the ratio of oxygenated hemoglobin versus the total hemoglobin in the blood. This method of monitoring blood oxygen levels requires a pulsating flow of blood [23]. A transcutaneous oxygen monitor measures the partial pressure of oxygen on the epidermis. The partial pressure of oxygen on the dermis is closely related to arterial oxygen levels [24]. Transcutaneous oxygen requires sufficient blood perfusion as well as diffusion of oxygen from the blood [25].

The arterial oxygen saturation (SaO_2) is a percentage value that represents the number of binding sites on hemoglobin that are bound with oxygen, therefore quantifying the oxygen in the blood [26]. The partial pressure of oxygen (PaO_2) is the measurement of the dissolved oxygen content in the arterial blood. $PtcO_2$ is directly correlated to PaO_2 and SpO_2 is directly correlated to SaO_2 [3].

The relationship between the SpO_2 percentage and PaO_2 is described graphically using the oxygen-hemoglobin dissociation curve as shown in Figure 1 [3]. This graph indicates that as the partial pressure of oxygen in the blood increases, the blood oxygen saturation also increases.

1.1.5 Need for Miniaturized Wearable Devices

There is a pressing need for miniaturized wearable devices that monitor respiration parameters remotely and continuously. Remote monitoring in the early stages of illness would provide healthcare providers with accurate data to create patient-specific treatment plans [27]. Early detection of respiratory diseases would minimize the burden on healthcare system resources, enabling patients to visit the hospital only

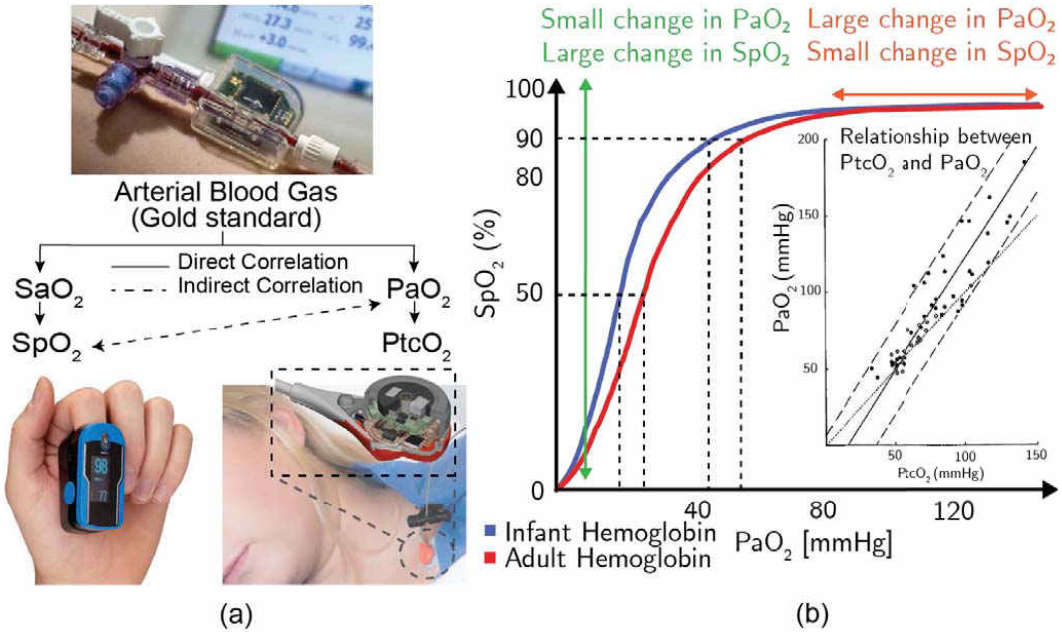

Figure 1: (a) Oxygenation measurement methods and their relation shown on an (b) oxy-hemoglobin dissociation curve [3].

when necessary [28]. This was especially important during the height of the COVID-19 pandemic, as resources were scarce. There was an extreme lack of personal protective equipment, hospital beds, staff, and ventilators [29]. Having the option to monitor symptoms remotely would allow patients to only go into the hospital only when necessary. This would have helped triage patients more accurately according to disease progression and severity. Creating a device to monitor respiration remotely would help manage and prevent similar scenarios from occurring in the future [29].

1.2 Transcutaneous Oxygen Sensors

1.2.1 How do Traditional Electrochemical Transcutaneous Oxygen Sensors Work?

Traditional transcutaneous oxygen sensors use electrochemical Clark electrodes. Clark electrodes are composed of platinum electrodes, a heating mechanism, and an oxygen-permeable membrane [30]. Clark electrodes are not suitable for wearable devices as the heating element affects overall feasibility. It causes the size of the device to increase, it can irritate the skin if used for continuous monitoring, and also has an

increased power requirement [31]. Clark electrodes also suffer from errors such as signal drift, variable response time, and unstable measurements [32].

1.2.2 How do Luminescence-based Transcutaneous Oxygen Sensors Work?

Using a luminescence-based sensing technique can eliminate the challenges that are faced with a traditional electrochemical Clark electrode. A recent wearable presented in [33], utilized a luminescent oxygen-sensing film to measure transcutaneous oxygen levels diffused through the skin. The film's material, platinum porphyrin (Pt-porphyrin), consists of functional groups known as fluorophores whose fluorescence is suppressed in the presence of O_2. When the film is excited with blue light (peak emission wavelength of 450 nm), the fluorophore is excited to a higher energy state. The molecule falls back to a lower energy state and emits a photon of red light (peak emission wavelength of 650 nm). If oxygen is present, it will quench this photon emission. This phenomenon can be seen in Figure 2. The partial pressure of O_2 around the film is inversely proportional to the intensity and lifetime of the emitted red light. The lifetime-based method is more reliable compared to pulse oximetry since it is less affected by optical path changes [33].

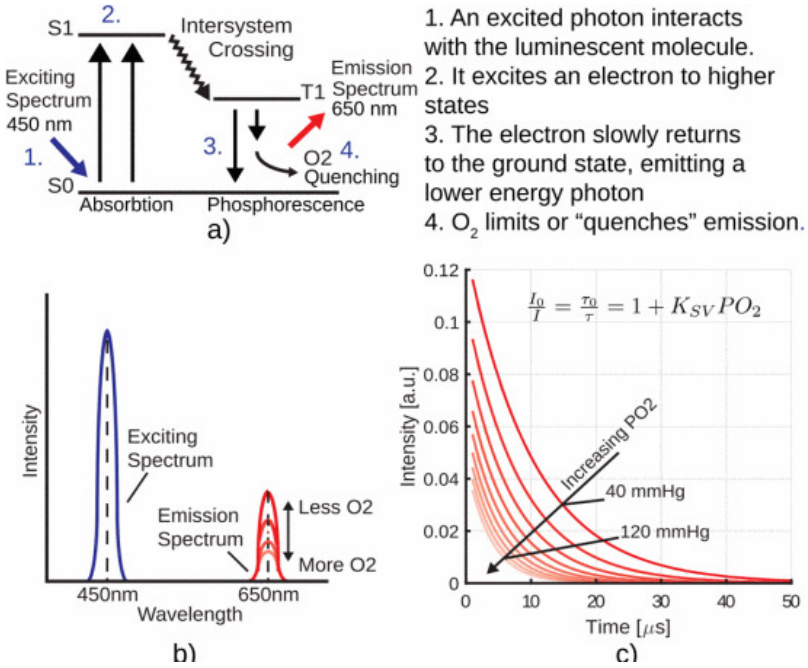

Figure 2: Electrical state diagram (a) wavelength shift (b), intensity of the emission quenched by O_2 [4] (c) intensity vs. time graph .

2 Project Overview

2.1 Project Organization

Our project consisted of three main phases: testing, signal processing, and PCB design. First, we created a testing plan to evaluate the current prototype. Our goal was to determine the optimal location to place the sensor on the human body for the most consistent and accurate readings. Initial pilot testing was conducted on a single human subject to narrow down potential locations for sensor evaluation. An ultrasound was used to aid in locating areas of high blood flow concentration. We then expanded the number of test subjects to ensure the sensor's success despite biological differences between subjects. Four participants were evaluated using the sensor prototype at several different locations. Following testing, the data were analyzed and processed using MATLAB. We used various signal processing techniques to eliminate outliers without losing the defining characteristics of the data. Simultaneously, we began creating new iterations of the printed circuit board (PCB) design to take steps toward reducing the size of the prototype for user comfort. The redesign incorporated a rigid-flex PCB which allowed the PCB to be folded, thus maintaining surface area while reducing the overall package size.

2.2 Test Implementation

To evaluate the accuracy and consistency of the device across various subjects, we completed a user study of the transcutaneous oxygen sensor. Based on the locations of prominent arteries and capillaries close to the skin, we conducted pilot testing on fourteen locations with a singular subject. Due to elements such as ease of testing and quality of data, the possible locations were narrowed down to the following: the thumb, top of the wrist, forearm, thigh, and shin. These five locations were tested independently on four different subjects. We compared the lifetime value and settling time of each location among subjects to evaluate the consistency of the device.

2.3 Signal Processing

The current state of packaging for the device can yield false readings and misleading data. The goal of signal processing is to remove prominent outliers and smooth deviations in the data without losing the signal's integrity. We explored multiple filtering methods and MATLAB functions to remove and replace outliers. This research focuses on testing these methods on our experimental data. We concluded that the Hampel filter was most successful at detecting outliers, and the fillmissing

function with the previous interpolation method was the most successful at replacing the outliers.

2.4 PCB Design

As the sensor's functionality was validated through the human subject tests, future modifications to the board can now be implemented for user comfort. The goal of redesigning the PCB is to reduce the space required to house the sensor. Thus, allowing the sensor to become more comfortable to wear. The original board layout was on a 100mm by 50mm board. The task was to convert the PCB to be flexible and have a package area of 40mm by 40mm or smaller. All components needed to be retained from the original design. The surface area could be retained despite the shrinking perimeter as multiple boards of the same dimension could be used and stacked on each other.

2.5 Project Challenges

Finally, we discuss various challenges the team navigated throughout the project. To improve the overall accuracy and wearability of the sensor, we recommended a variety of improvements.

3 Background Research

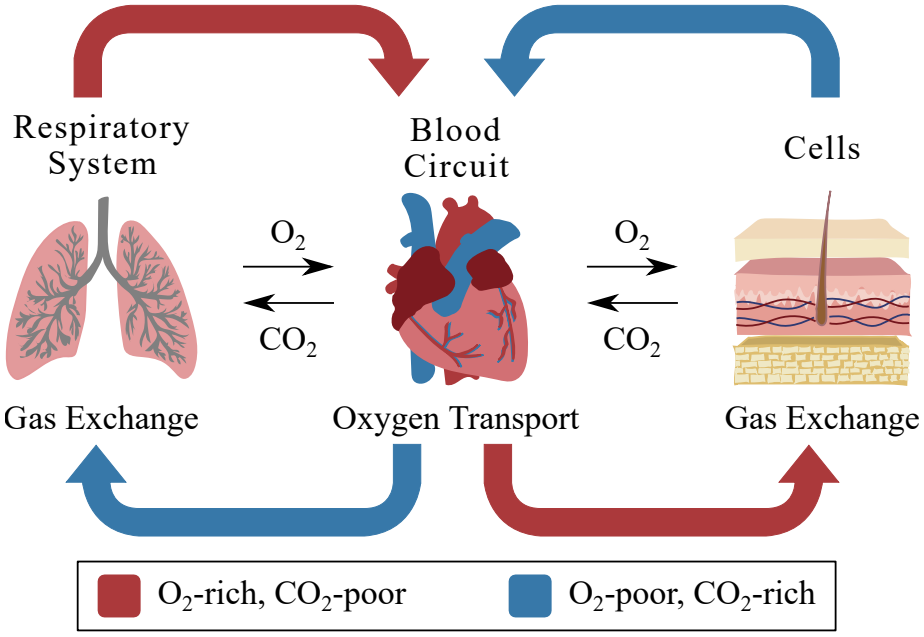

Figure 3: Oxygenation and circulation of blood in the body [5].

3.1 Circulatory System

The circulatory system is responsible for delivering oxygen (O_2) to tissues around the body. This process is depicted in Figure 3. Blood is oxygenated in the lungs and then circulated around the body through the blood vessels. The circulatory system is responsible for oxygen delivery from the red blood cells to the tissue cells [34]. This exchange of nutrients and oxygen is known as micro-circulation and involves arterioles, capillaries, and venules [34]. Oxygen delivery is administered by the capillaries, which are small blood vessels that branch off from arteries. As the blood flows through the capillaries, oxygen diffuses to the tissues. The oxygen content in the blood is highest on the arteriole end of the capillary. A representation of this micro-circulation process is shown in Figure 4 [6].

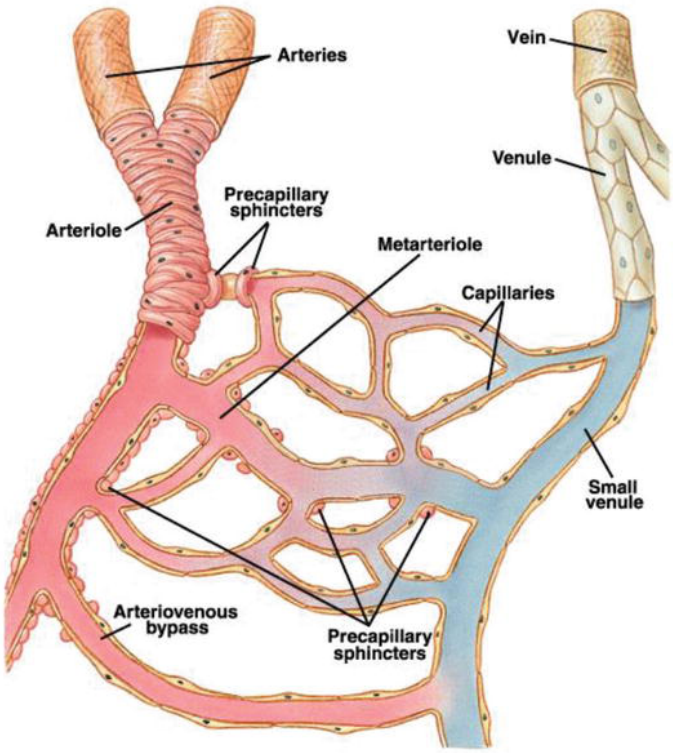

Figure 4: Micro-circulation within the circulatory system [6].

3.2 Physiological Factors

3.2.1 Dermal Perfusion

Dermal perfusion is the flow of blood to the dermis. This blood flow impacts transcutaneous oxygen levels. Transcutaneous oxygen is a measurement of the oxygen delivered to the skin from the underlying tissues [20]. Many factors impact the amount of blood flow to the dermis as well as the rate at which blood is circulating. Blood perfusion is affected by changes in the cardiovascular system, hormonal function, and circulatory function. Therefore, poor blood perfusion or changes in blood perfusion may be indicators of health defects [35].

3.2.2 Circulatory/Cardiovascular Function

Circulatory/Cardiovascular function directly impacts dermal perfusion. Dermal perfusion is related to the ability of the heart to pump blood through the vessels around the body. The cardiac output is a measure of this and is defined as the amount

of blood pumped each minute by the heart. Changes in the cardiac output affect the blood pressure and the rate of blood flow [36]. Poor blood circulation directly impacts dermal perfusion. Conditions, such as coronary and carotid artery disease, cause the narrowing of the arteries and blood vessels resulting in poor circulation of blood [37] [38]. Environmental factors such as cold air result in the arteries narrowing, preventing heat loss to maintain the body's core temperature [39]. Treatments for certain conditions also result in the narrowing of blood vessels facilitated by vasoconstriction medications such as angiotensin-converting enzyme (ACE) inhibitors and nitrates [40].

3.3 Oxygen Diffusion

3.3.1 Epidermal and Subcutaneous Fat Thickness

A greater diffusion distance results in less oxygen from the capillaries diffusing to the epidermis, reducing $PtcO_2$ [41]. The diffusion distance between the capillaries and the epidermis is increased due to factors such as subcutaneous fat and epidermal thickness [41]. Epidermal thickness and distribution of fat vary between body locations and between individuals.

3.3.2 Capillary Density

A study has suggested that $PtcO_2$ depends on the capillary density [41]. The capillary density is defined as the number of capillaries per unit of cross-sectional area of muscle [42]. Maintaining a highly perfused capillary density will result in smaller diffusion distances from capillary to tissue [43]. The density of capillaries in the skin varies between individuals and differing body locations [44]. Capillary density can increase in athletic individuals, this is known as capillarization [45]. Capillarization increases the muscle-blood surface area to increase exercise capacity [45].

3.4 Transcutaneous Sensor Locations

Locations that are assumed to be the best for transcutaneous oxygen measurements are those that have thin skin and are highly vascularized. A research study suggested that the palm of the hand provides the most consistent transcutaneous measurements, possibly due to the high vasculature [46]. Other locations such as the forearm, chest, and abdomen, have been reported as optimal locations for testing. However, these locations were tested using applied heat to increase blood flow and diffusion [47]. Another study conducted using a transcutaneous monitor has suggested that the

anterior chest is not an optimal place as this sensor site had lower reading when compared to the hand and arm [48]. Locations for infants are different compared to adults. The primary location for newborn intensive care unit (NICU) patients and infants is the upper chest [49]. Locations such as the ear have been investigated as this location does not risk detachment during movement [49]. To further investigate the best oxygen locations, the team tested multiple locations on the body. These locations were tested without the application of heat [50]. The initial locations for testing included the cheek, neck, upper back, collarbone, bicep, forearm, wrist, thumb, chest, thigh, and shin.

3.5 Decontamination and Sterilization of Sensor Packaging and Film

It is important that all components of the sensor are able to be decontaminated to remove microbials on the surface of the device. Research has been conducted that is currently in the beginning phases and has suggested promising results. Important parts of the decontamination process include mitigating risk to the integrity of the sensor. It is important to not compromise the film accuracy and the sensor's electrical components. The film data sheet indicates that the film can be in contact with ethanol and not risk reduction in accuracy [51]. Ethanol as a sterilizing agent has been used effectively in healthcare [52]. Along with the film, research suggests ethanol is an effective method of cleaning electronics. Through the use of pure-ethanol, electronics can be decontaminated with minimal risk to electrical component damage [53].

Other methods of decontamination that are compatible with electronics include Ultraviolet C (UVC). No research has been conducted on its impact on the film; however, UVC has promising results for electronic decontamination. In another study conducted, 87% of the surfaces had a reduction in microbes [54]. It was also determined that the amount of decontamination was dependent on the exposure time to the UVC [54].

Methods of decontamination that have been studied for current market devices include neutral electrolyzed water. In a study to prevent infection while using a transcutaneous oxygen monitor, it was found that exposure to electrolyzed water removed microbes on the surface of the sensor [55]. While this research is still in the early stages, it is important to determine methods of decontamination and the research has indicated multiple methods to be further investigated.

Methods of sterilizations are important to consider for initial distribution of the sensor. Initial research has been conducted to determine the best methods of sterilization for the sensor. The initial research indicated that chloride dioxide is the best

Table 1: Sterilization Methods and Their Compatibility with Electronics

Sterilization Method	**Problematic Parameters**	**Compatibility**
Autoclave Steam	Temperature, humidity	Can affect floating-gate memory cells (EEPROM)
Ethylene Oxide	Flammability carcinogen	The vacuum can affect embedded batteries
Chloride Dioxide	None	There are no adverse effects on electronics or batteries
Vaporized Hydrogen Peroxide	Vacuum	The vacuum can affect embedded batteries
Hydrogen Peroxide Plasma	Vacuum, plasma discharge	The RF energy required to generate the plasma may not be compatible to semiconductors
Gamma Ray	Radiation, nuclear waste	The radiation can damage semiconductors that are not designed for
Electron Beam	Radiation	The radiation can damage semiconductors that are not designed for exposure

option of sterilization for electronics and batteries [56]. As shown in Table 1, two sterilization methods have issues with embedded batteries, therefore, if batteries were removed before sterilization, these are also options to consider [56].

4 Test Implementation

The team first developed a regimented formula to standardize testing. During implementation, volunteers helped verify the accuracy of the sensor. We selected various locations on the human body for testing based on artery locations.

4.1 Methods

We conducted pilot testing using the sensor on one subject. The team selected the initial locations based on research on capillary-dense areas and major arteries. Results from pilot testing can be seen in Appendix 8 and testing locations are shown in Table 2.

Table 2: Pilot Testing Locations

Location	**Corresponding Artery**
Thumb	Digital Artery
Lower Thumb	Digital Artery
Bottom of Wrist	Ulnar Artery
Top of Wrist	Ulnar Artery
Bicep	Brachial Artery
Clavicle	Subclavian Artery
Neck	Carotid Artery
Ear	Superficial Temporal Artery
Cheek	Traverse Facial Artery
Chest	Coronary Artery
Abdomen	Iliac Artery
Thigh	Superficial Femoral Artery
Shin	Tibial Artery

After an initial assessment, we narrowed down the measurement locations to the following: the top of the wrist, forearm, thigh, thumb, and shin. Before conducting the test, a portable ultrasound was used to detect the closest artery to find the ideal placement of the sensor. An example of our ultrasound measurements can be seen in Figures 5 and 6.

Our team completed the next phase of the user study after narrowing down potential test locations. Multiple subjects were tested to evaluate the repeatability and accuracy of the sensor. Medical-grade accuracy and repeatability between subjects are crucial

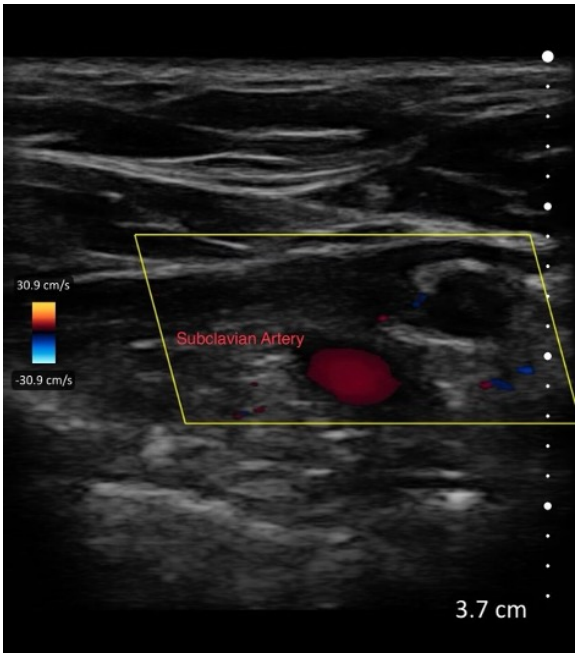

Figure 5: Ultrasound of subject's subclavian artery.

for the sensor to have a future in remote health monitoring. The team aimed to locate successful testing locations, where there were relatively small standard deviations between lifetime value measurements among peer locations. The general setup of the tests is in Figure 7, where the PCB was placed directly on the subject's skin.

Testing was conducted using a routine procedure:

1. Clean skin with an alcohol wipe
2. Take 6 ambient air measurements
3. Fix the sensor to the skin
4. Collect continuous data points

This repetition in testing allowed for consistent measurement practice. The sensor's accuracy relied on the O_2 quenching film contacting the patient's skin. Therefore, it was important that the subject's skin was clean before the testing process began as not to corrupt the data measurements. The sensor measured ambient air before contact with the skin was made. This practice ensured the sensor was functioning as expected. Air consistently reported a lifetime value between 12μs and 14μs. Additionally, the

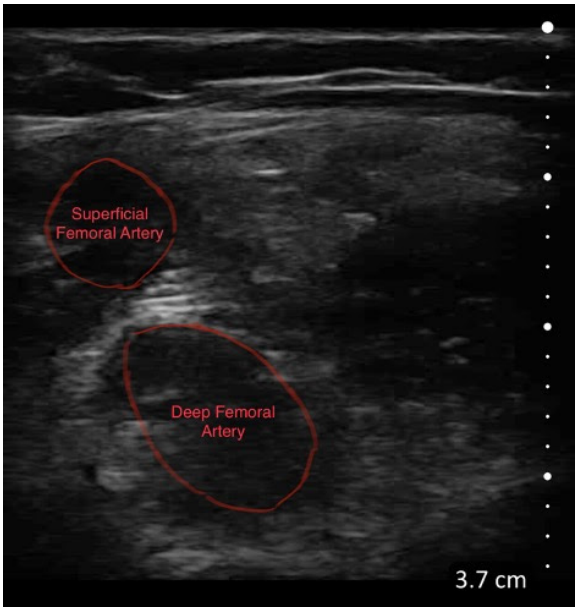

Figure 6: Ultrasound of subject's femoral arteries.

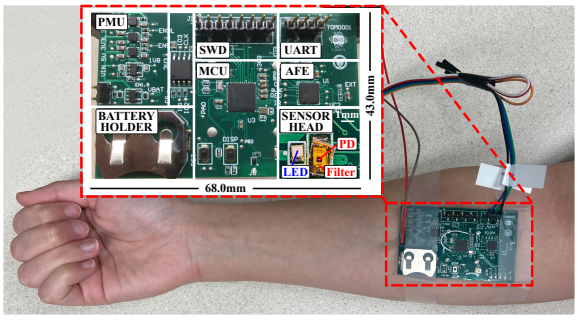

Figure 7: Sensor layout and placement on the forearm (shown as an inset, the sensor head is located on the board's bottom side).

ambient air measurements served as a reference point for future data processing and adjustments.

As the current version of the prototype does not have an air tight-reservoir, a certain amount of pressure is required to prevent ambient air rush-in into the sensor, ensuring accurate readings. Based on the body part, the method to secure the sensor to the skin changed. Typically, an adhesive helped maintain consistent pressure and ensure that the PCB remained fixed to the skin. However, locations such as the thumb were more successful without using tape. Due to the thumb's smaller surface

area and shape, it was easier to apply pressure from above. Using a clamp to hold the sensor upright, the subject placed their thumb on the LED side of the PCB and held it down as the readings were taken.

After maintaining successful contact, the sensor could collect accurate measurements. The UART interface communicates between the PC and the sensor. A MATLAB script controlled the sensor by modulating the power source on and off. The experiment utilized a time interval of 10 seconds between sensor readings. MATLAB would populate a graph of lifetime values versus time with each new data point. The data consistently showed a line trending upwards before reaching a stabilization point where the data would flatline. At this point, we assumed the oxygen quenching film had reached equilibrium and accurately reported the lifetime value measurement. This measurement was recorded along with the settling time of how long it took for the sensor to reach stability.

4.2 Results

The lifetime values of the thumb, forearm, wrist, shin, and thigh were measured on four different test subjects. The distribution of settling times and associated lifetime values of each body location is represented in Figures 8a and b.

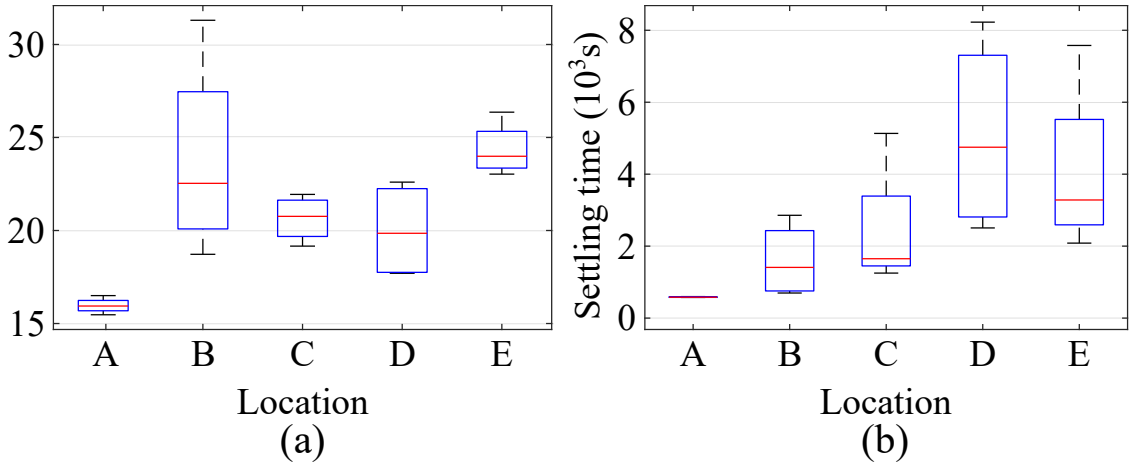

Figure 8: Distribution of experimental data among locations for (a) lifetime value and (b) settling time (locations are denoted as: A - thumb, B - wrist, C - forearm, D - thigh, and E - shin).

The thumb, wrist, forearm, thigh, and shin varied in terms of settling time and τ value across four subjects. Certain locations, like the thigh and wrist, showed

Table 3: Settling Times and Lifetime Values for Each Subject by Location

	Subject A		**Subject B**		**Subject C**		**Subject D**	
Testing Locations	Settling time (s)	τ (μs)	Settling time (s)	τ (μs)	Settling time (s)	τ (μs)	Settling time (s)	τ (μs)
Thumb	574	16.50	576	14.10	584	15.47	598	15.98
Wrist	2857	18.72	2006	21.45	812	23.60	697	31.30
Forearm	2650	20.20	1251	21.32	2650	21.94	5133	19.16
Thigh	8226	17.70	3115	21.19	6384	22.6	2506	17.80
Shin	2084	23.03	3100	24.30	3466	26.36	7578	23.68

significantly more variation across test subjects compared to the thumb. The thumb showed the lowest variability in both settling time and value. In comparison, the thigh resulted in the largest variation of settling time 2,500–8,200 s, and the wrist had the most variation in τ values 19–31 μs.

Out of the five measurement locations, the thumb reached its settling point the fastest, reporting an average of 583 s and a standard deviation of 10.69 s. The thumb showed the smallest variation in settling time ranging from 574–598 s, as well as the least variation in lifetime value from 14.10–16.50 μs. The average value for the lifetime value of the thumb was 15.51 μs. All settling times are recorded in Table 3.

In addition, we evaluated the reproducibility of the experiment by collecting three data sets for one body location. The testing took place with uniform conditions. These conditions also include testing on sequential days at the same time each day with no eating prior to the trials. However, physical activity, sleep duration, and sleep quality were not tracked. Figure 9a compares the stabilized lifetime values for one human subject for three days. The first trial reported a setting time of 598 s with a τ value of 15.98 μs. The second trial reported a settling time of 607 s with a τ value of 14.3 μs. The third trial reported a settling time of 621 s with a τ value of 14.4 μs.

4.3 Challenges

Throughout the testing process, we encountered different obstacles. The sensor needed constant pressure throughout the testing. Without consistent pressure, the sensor would not make contact enough with the skin causing lifetime readings to drop. When the lifetime value dropped to the value of ambient air, it indicated that the film had momentarily lost contact with the skin. Alternatively, too much pressure caused lifetime values to spike.

Based on initial testing, lifetime values directly correlate to oxygen readings, seen in Figure 10. However, the lifetime values theoretically hit a maximum of around 30 μs. Therefore, anytime the data was above 30 μs, it was an indication that the

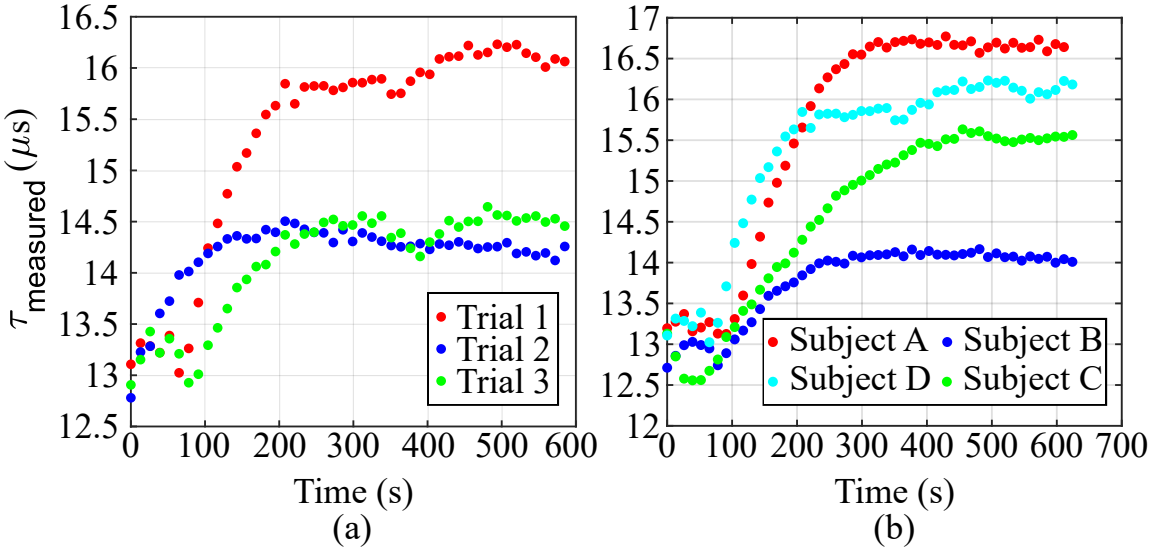

Figure 9: Lifetime value over time for (a) the thumb of Subject D on three separate days and (b) the thumb of four human subjects.

value could not be converted into an oxygen reading. This constraint presented a challenge as the data would occasionally settle above the anticipated 30 μs maximum. Each time the measurements settled above 30 or exhibited outlier values, we restarted testing.

Additionally, we found that each body location required a different amount of time to settle. Due to thicker tissue increasing distance from blood flow, the oxygen quenching film took longer to reach equilibrium. The thigh location frequently exhibited these challenges, requiring one subject to wait 8000 seconds, just over two hours, for a measurement to stabilize.

Different environmental factors also altered the readings of the sensor. When the subjects tested after eating, it was sometimes more difficult for lifetime values to stabilize and would instead fluctuate to a greater degree. This is likely due to how digestion alters the distribution of oxygen in the body. Thus, after this discovery, the subjects were unable to eat before testing.

The sensor needed to make complete contact with the skin, as the PD needed to be in total darkness for an accurate measurement. As the measurement technique depends on measuring reflected light and utilizes PDs, any escaped light can induce measurement errors. This circumstance was challenging because if a subject jostled the sensor with any minor movement and broke contact, the PDs could not measure properly. Often the sensor would begin reporting values close to ambient air if the PDs were exposed. Under this scenario, we restarted testing due to errors in the data

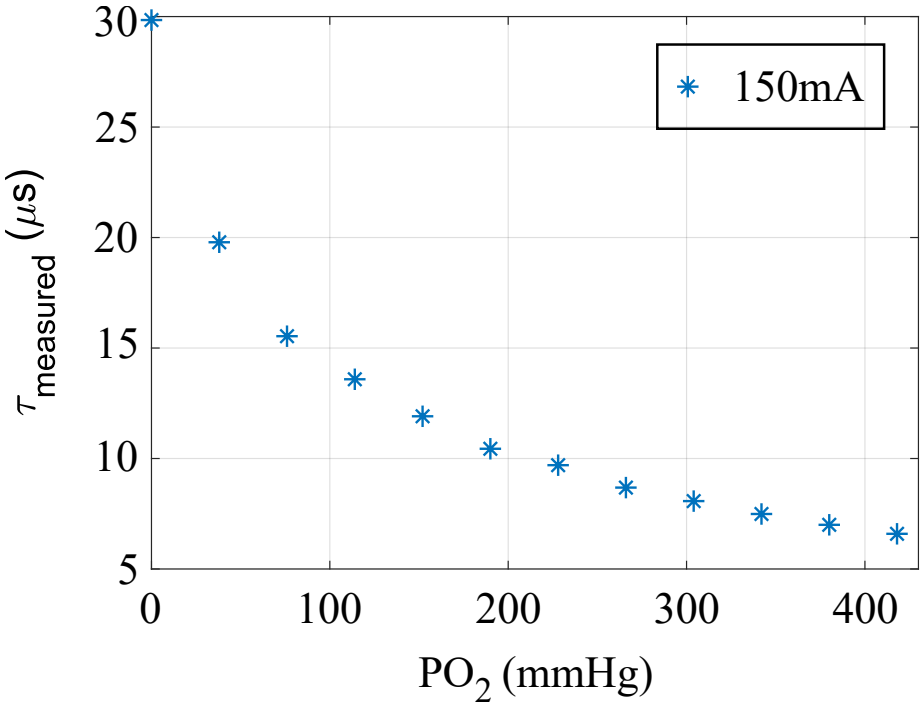

Figure 10: Lifetime value versus partial pressure of oxygen plot generated from gas sweep.

history and subsequent graphs.

4.4 Discussion

To determine the optimal location for measuring $PtcO_2$, we used parameters such as settling time, consistency, and variation in lifetime measurements. The data collected from the four subjects represented in Figures 8a, b, and Figure 9b demonstrate that the sensor is capable of accurately measuring the lifetime value for a variety of different body locations. Moreover, Figure 9a demonstrates the sensor's ability to reproduce data.

Based on the results from the four subjects, the thumb reported the shortest settling time and smallest variation in lifetime value. Determining the optimal location will vary according to the application of the sensor as key criteria will change. For example, in one use, a smaller settling time may be preferred, or in another application, specific packaging constraints may limit location options.

Although the four subjects exhibited a range of different settling times and lifetime values, slight variations are expected. The genetics of each subject differed, affecting

the results. To ensure consistent readings across a diverse range of subjects, a computational model can be trained to refine the data. Future work can consist of creating a computational model to personalize the results. Additionally, the packaging on the prototype must be finalized to ensure consistent pressure and contact with the sensor. Improving the data collection process will account for the biological differences between individuals and adjust measurements accordingly.

There is a broad range of $PtcO_2$ values obtained by measuring different locations on the body. This indicates biological variability impacts transcutaneous oxygen measurements. The findings from this research suggest that different locations on the body result in varied transcutaneous oxygen measurements. Slight variations in results are expected as the genetics of individuals differ between subjects. Our measurements agree with the previous studies performed using commercial transcutaneous oxygen sensors. The optimal location will depend on the commercial application. Criteria and restrictions will vary according to the use.

5 Signal Processing

5.1 Motivation

The current stage of packaging for the device can cause misleading data. For example, if you move your finger slightly from the sensor and the film is exposed to ambient air, it will cause a rush of oxygen (O_2). Which results in the rapid decline of decay time value, yielding a false reading. An example of this disrupted data is in Figure 11 below.

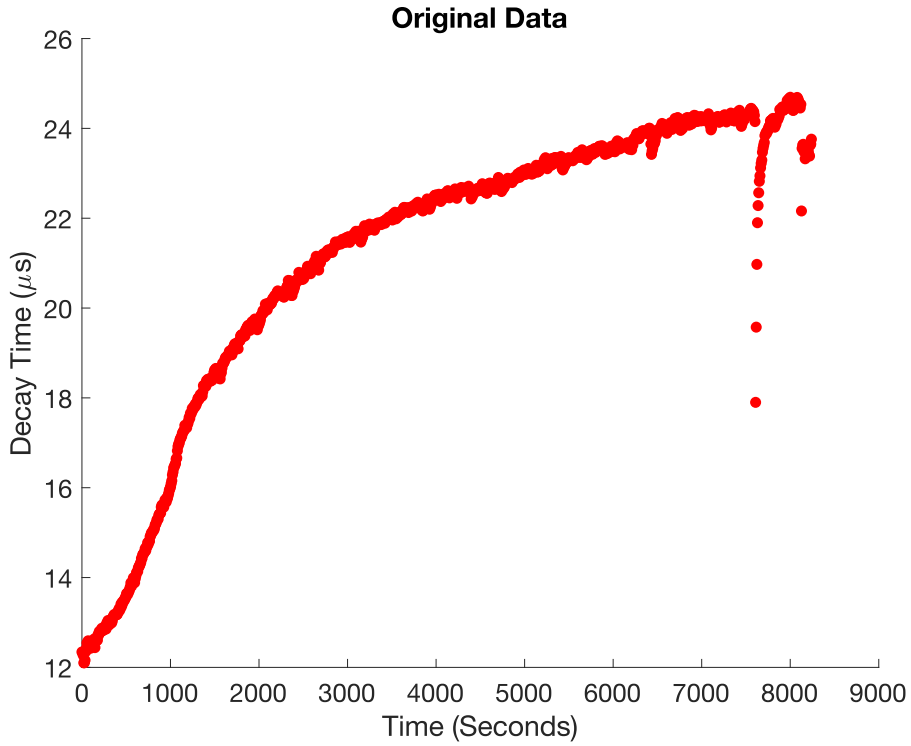

Figure 11: Example experimental data displaying O_2 rushing.

The goal of signal processing is to remove prominent outliers and smooth deviations in the data without losing the integrity of the initial signal. For example, Figure 12 depicts a signal with small increases and decreases in decay time. It is important that the algorithm removes outliers while simultaneously preserving these original data trends. These small fluctuations indicate important details about a patient's health status. This information can help healthcare professionals determine more

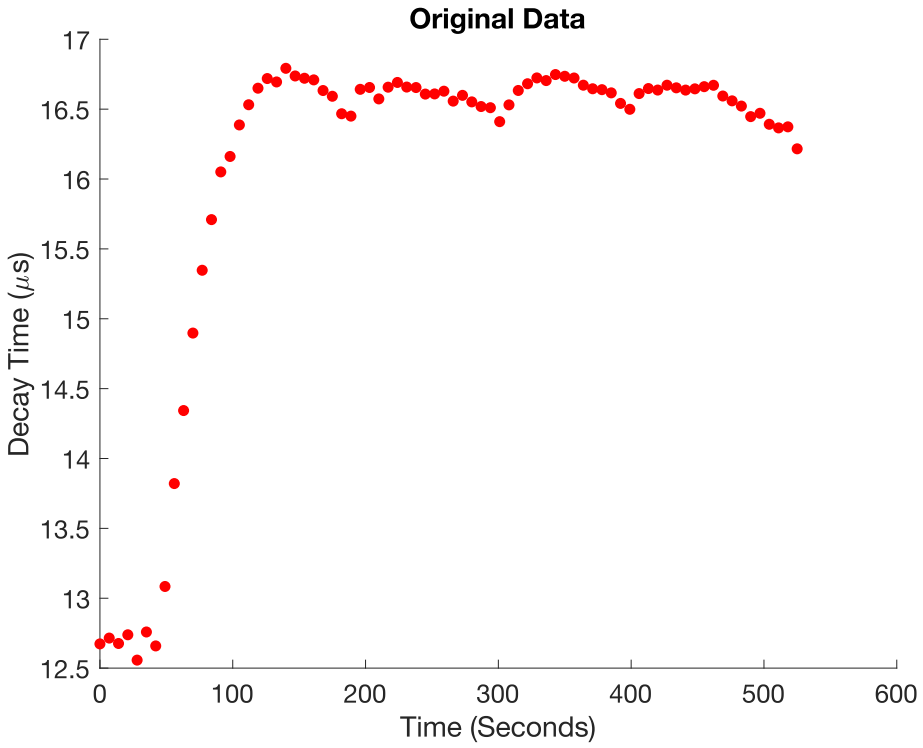

Figure 12: Example experimental data displaying small increases and decreases in decay time.

accurate conclusions regarding a patient's health.

5.2 Methods

MATLAB has a variety of filters and other functions that detect and eliminate misleading data. To compare the success of each filter method, the original and filtered data were plotted on top of each other. The Hampel filtering method proved the most successful at detecting and removing the outliers. Then, the "fillmissing" function was used with the "previous" interpolation method to replace the outliers. The team tested these filters and functions on sample data from initial experiments to validate the algorithm's functionality on diverse data sets.

5.2.1 Outlier Detection

Initially, the team looked at different filter methods to detect, remove, and replace outliers. Out of all filter methods, the Hampel filter is the best at removing outliers while maintaining the integrity of the primary signal.

Hampel Filter The Hampel filter utilizes a property known as the Hampel Identifier, an adaptation of the three-sigma rule [57]. The three-sigma rule is also known as the empirical rule or the $68 - 95 - 99.7$ rule, where almost all the data lies within three standard deviations from the mean. For each sample, the filter computes a window of the sample taking in the current sample value and $(k - 1)/2$ adjacent samples. The filter replaces a sample with the median if the sample differs from the median greater than the threshold value multiplied by the standard deviation [57].

The basic structure of a Hampel filter is as follows: [y, j, xmd, xsd] = hampel(x, k, nsigma) [58], where "y" is the output filtered data, "j" is a logical vector that returns true at all the points of the original vector that are outliers, "xmd" represents the local medians for each element of x, "xsd" represents the estimated standard deviations for each element of x, "x" is the input vector, "k" specifies the number of neighbors on both sides of each sample of x, "nsigma" represents the number of standard deviations that the sample of x must vary from the local median for it to be replaced with the local median [58].

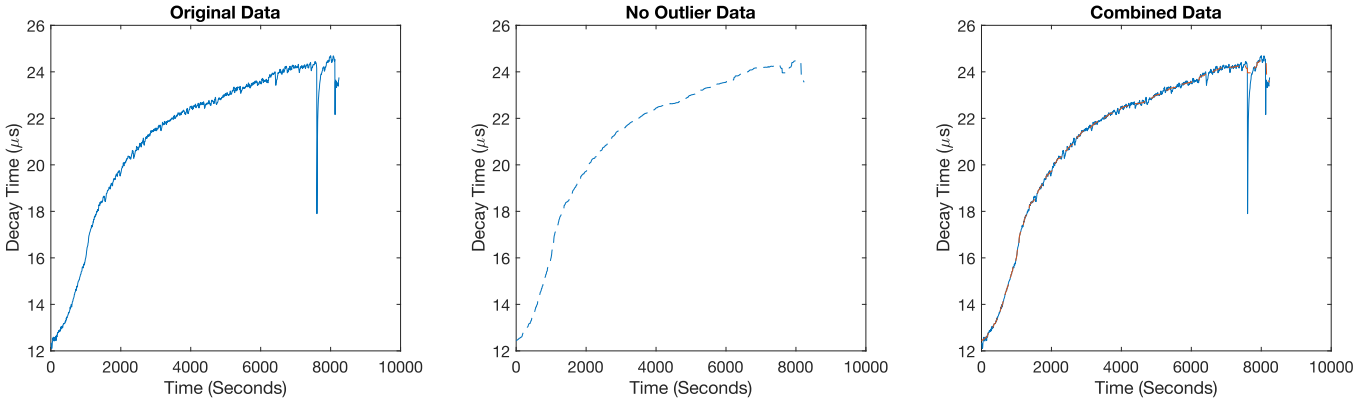

Figure 13: Effect of Hampel filter on outlier data.

An example of the Hampel filter is in Figure 13. The image on the left depicts the original data set. The image in the middle shows the modified data set using a Hampel filter with a k value of 20 and a nsigma value of 0.1. The image on the right

shows both the left and middle datasets plotted on top of each other to depict the overall changes made by the filter.

Rmoutliers The basic structure used for rmoutliers is as follows: [B,TFrm] = rmoutliers(A, movmethod, window) [59], where "B" is the output filtered data, "TFrm" is a logical vector representing the data removed from A, "A" is the input vector, "movmethod" has two possible inputs: "movmedian" and "movmean," "movmedian" defines outliers as more than three local scaled median absolute deviations from the local median over a specific window length, "window," "movmean" defines outliers as samples that differ more than three local standard deviations from the local mean over a specific window length, "window," "window" is window length. To remove outliers this filter uses either the movmean or movmedian movmethod [59]. For example, rmoutliers(A, "movmean", 7) removes data points that are more than three local standard deviations from the local mean within a seven-element window.

An example of the rmoutliers function is in Figure 14. The image on the left depicts the original data set. The image in the middle shows the modified data set using the function rmoutliers with a movmethod of movmedian and a window length of 20. The image on the right shows both the left and middle datasets plotted on top of each other to depict the overall changes made by the filter.

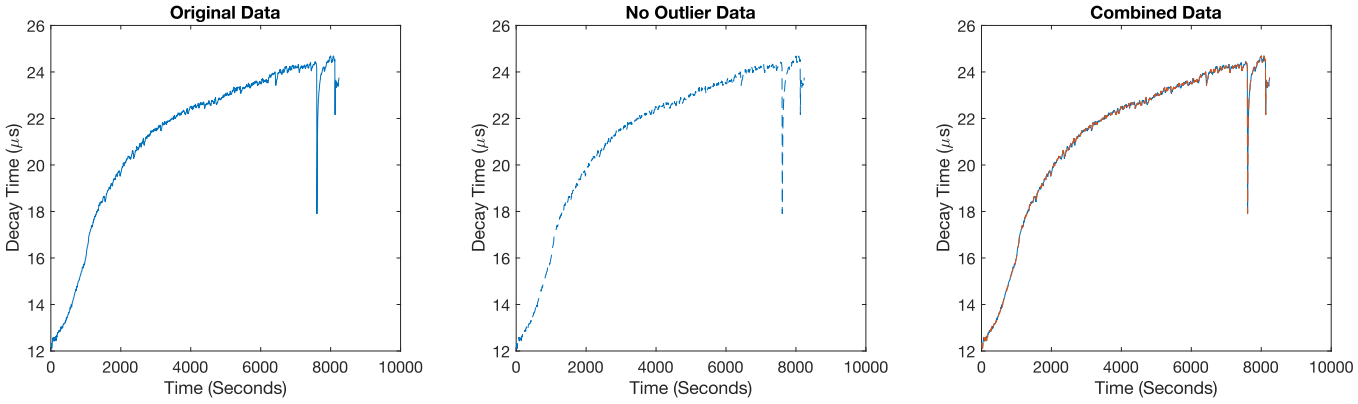

Figure 14: Effect of rmoutliers on outlier data.

Filloutliers The basic structure used for filloutliers is as follows: [B,TF] = filloutliers(A, fillmethod, movmethod, window) [60], where "B" is the output filtered data, "TF" is a logical array that represents the position of elements of B that were previously outliers, "A" is the input vector, "fillmethod" has nine possible inputs:

"center," "clip," "previous," "next," "nearest," "linear," "spline," "pchip," and "makima." These methods all represent different ways that the outliers can be filled. "movmethod" has two possible inputs: "movmedian" and "movmean." "movmedian" defines outliers as more than three local scaled median absolute deviations from the local median over a specific window length, "window." "movmean" defines outliers as samples that differ more than three local standard deviations from the local mean over a specific window length, "window." To remove outliers this filter uses the movmethod to identify outliers and fillmethod to replace outliers [60]. For example, filloutliers(A, "next", "movmean", 7) removes data points that are more than three local standard deviations from the local mean within a seven-element window and replaces them with the next non-outlier value in the data set.

An example of the filloutliers function is in Figure 15. The image on the left depicts the original data set. The image in the middle shows the modified data set using the function filloutliers with a fillmethod of linear, movmethod of movmedian, and a window length of 80. The image on the right shows both the left and middle datasets plotted on top of each other to depict the overall changes made by the filter.

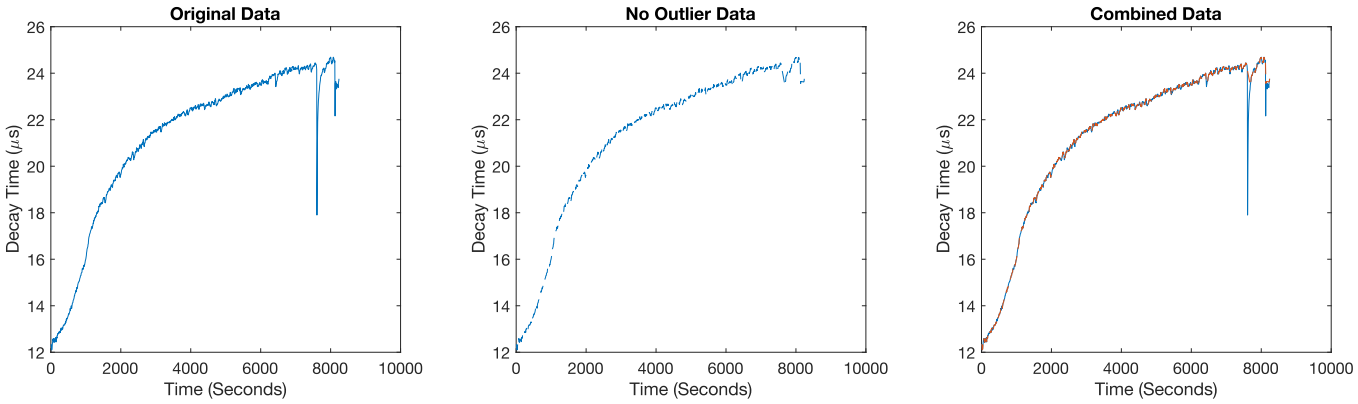

Figure 15: Effect of filloutliers on outlier data.

Medfilt1 The basic structure for medfilt1 is as follows: y = medfilt1(x,n) [61], where "y" is the output filtered data, "x" is the input vector, and "n" is an nth-order one-dimensional median filter. To remove outliers this filter applies an nth-order filter to the input vector x. For example, this medfilt1(x, 7) smooths the data with a 7th-ordered median filter [61].

An example of the medfilt1 function is in Figure 16. The image on the left depicts the original data set. The image in the middle shows the modified data set using the

function filloutliers with a 20th-order one-dimensional median filter. The image on the right shows both the left and middle datasets plotted on top of each other to depict the overall changes made by the filter.

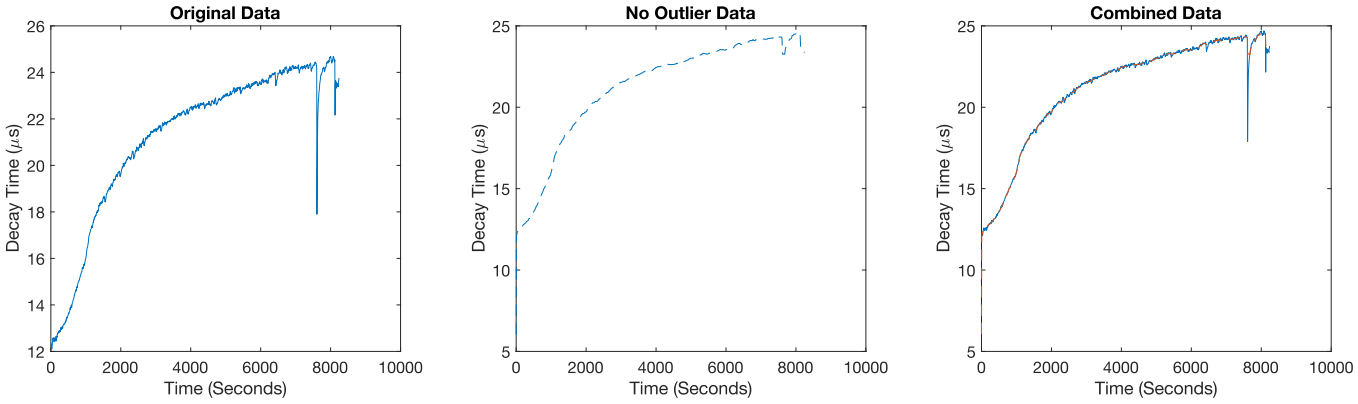

Figure 16: Effect of medfilt1 on outlier data.

Moving Average Filters There are multiple ways to implement moving average filters in MATLAB. The first method utilizes the 1-D digital filter function. The basic structure for the filter function is as follows: y = filter(b,a,x) [62]. Using numerator and denominator coefficients b and a, a rational transfer function filters the input data x. The team utilized the following equation to create a moving average filter:

$y(n) = (1/windowSize) * (x(n) + x(n-1) + ... + x(n-(windowSize-1)))$ [61]

An example of this moving average filter is in Figure 17. The image on the left depicts the original data set. The image in the middle shows the modified data set using the function filter. The "b" coefficient is $(1/windowSize) * ones(1, windowSize)$. The "a" coefficient is 1. The window size for this function is 20. The image on the right shows both the left and middle datasets plotted on top of each other to depict the overall changes made by the filter.

The second method also uses the filter function [63]. However, The team used this equation to create a moving average filter:

$a(1)y(n) = b(1)x(n) + b(2)x(n-1) + ... + b(N_b)x(n-N_b+1) - a(2)y(n-1)$
$-... - a(N_a)y(n-N_a+1)$ [63]

An example of this moving average filter is in Figure 18. The image on the left depicts the original data set. The image in the middle shows the modified data set using the function filter. The "b" coefficient is $[1/4, 1/4, 1/4, 1/4]$. The "a" coefficient

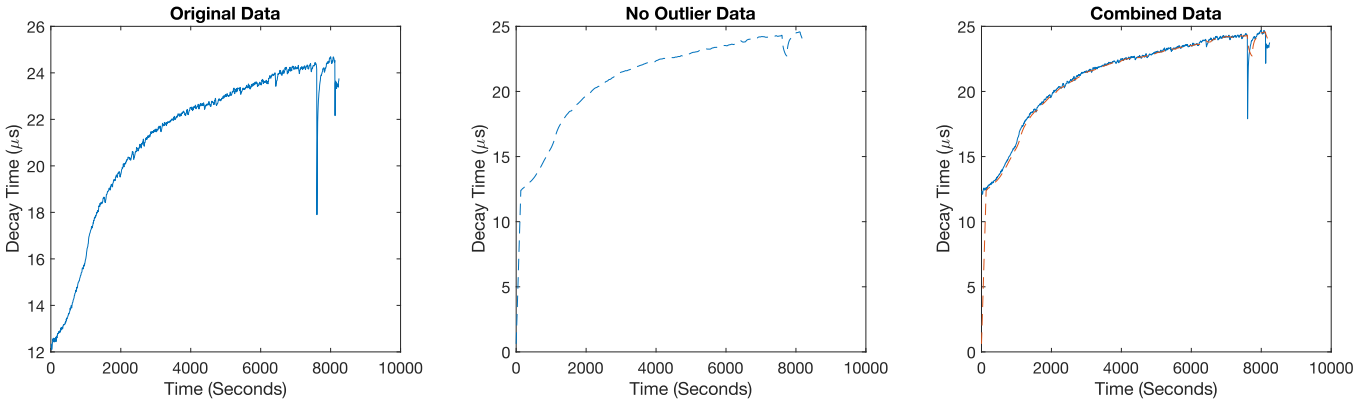

Figure 17: Effect of moving average filter on outlier data sets using method 1.

is 1. The image on the right shows both the left and middle data sets plotted on top of each other to depict the overall changes made by the filter.

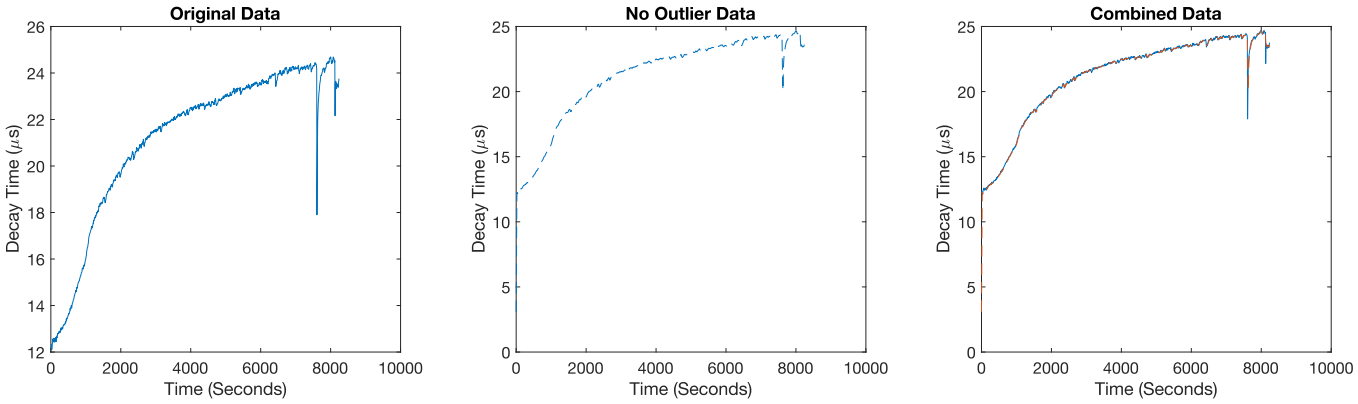

Figure 18: Effect of moving average filter on outlier data sets using method 2.

5.2.2 Replacing Outliers

The "fillmissing" function in MATLAB replaces outlier data. The basic structure for fillmissing is as follows: F = fillmissing(A,method) [64], where "F" is the output data, "A" is the input vector, and "Method" is the fill method that replaces the outlier data. "Method" has seven possible inputs: "previous," "next," "nearest," "linear," "spline," "pchip," and "makima." Specifically, this function fills missing data (or data classified

as not a number (NaN)) with the identified interpolation method [64]. To use this function with outlier data, replace the outlier values with NaN.

5.3 Results and Discussion

The Hampel filter was the most accurate at smoothing data compared to other filtering methods (as shown in Figures 13, 14, 15, 16, 17, and 18). However, it is challenging to standardize one set of parameters to apply to diverse data sets. Instead, the team took a two-step approach. First, the Hampel filter was used to identify and remove the outliers. Then, the fillmissing function was used to replace the outliers with a specified interpolation method.

In more detail, the input parameters of the Hampel filter were fine-tuned to accommodate a more diverse data set. The team utilized a k value of 35 and a nsigma value of 3.5. To ensure the filter detected outliers that were considered distinctly different from the original data the nsigma of 3.5 was standard. The team chose a high k value of 35 as it is important when dealing with biomedical data to preserve overall data trends. This data can give critical information about the patient's medical status. Figure 11 represents a unique outlier case of O_2 rushing. As you can see in the top image of Figure 19, the Hampel filter successfully detected outliers in the data. The outliers are identified with square boxes. The bottom image in Figure 19 shows how the fillmissing function replaces the outliers using the previous interpolation method.

To use the fillmissing function in MATLAB, the outliers identified by the Hampel Filter were cast as NaN. The "previous" interpolation method replaced outlier data with the previous nonmissing value.

The team then applied this algorithm to test data from our previous experiments. Figure 20 portrays data with small increases and decreases in the decay time values. Maintaining the integrity of these fluctuations can be important for informing decisions about a patient's health. As you can see, the algorithm successfully identified outliers while preserving the original data trends.

Next, an algorithm was applied to a set of data that stabilized normally. Figure 21 portrays the data. As you can see, the algorithm was able to identify that there were no outliers. This further validates that our algorithm works on diverse data.

Again, the team applied this algorithm to another data set from our previous experiments. Figure 22 portrays data with a decrease in decay time value at around 1300 seconds. It is important that this dip was not recognized as an outlier, as small fluctuations such as this can be critical for informing decisions about a patient's health.

The team applied this algorithm to data with a system error (values reaching the

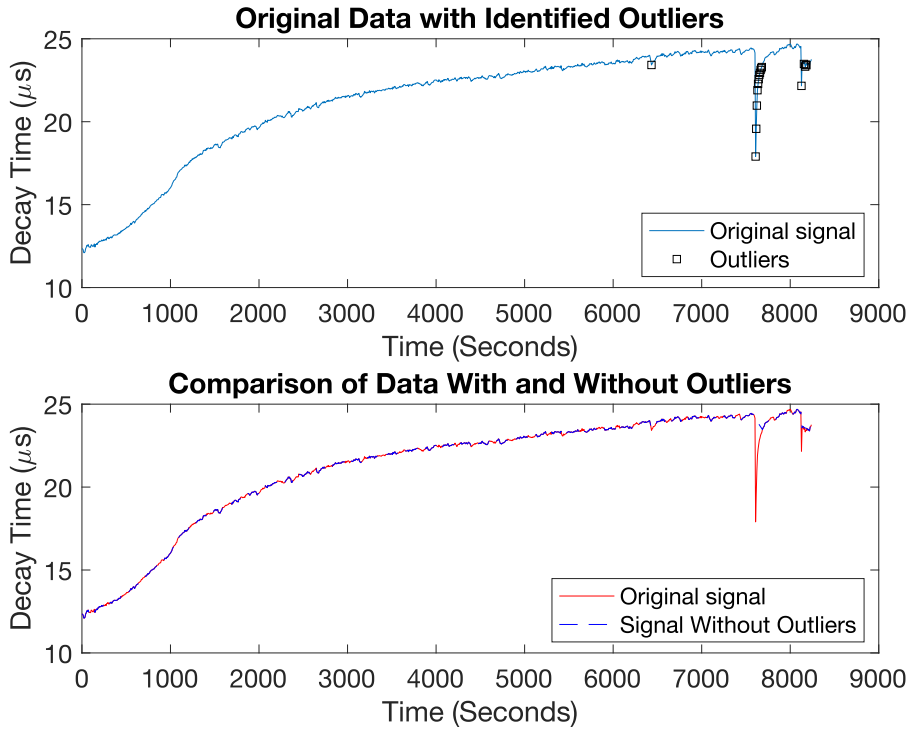

Figure 19: Outlier detection and replacement algorithm successfully applied to outlier case of O_2 rushing.

negatives). Figure 23 portrays data with a large decrease in decay time to negative values at around 42 seconds. It is important that this dip was recognized as an outlier, as negative decay values in this application indicate a system error. The algorithm was able to remove the outlier.

The previous and linear interpolation methods can be used with this algorithm. However, the validity of four common methods: previous, linear, spline, and pchip were tested. Figure 24 and Figure 25 utilize data from Figure 11. All four interpolation methods were tested on this data set.

At first, all signals look to have a similar effect. However, when the signals are overlaid on top of each other, there are subtle differences in the data, as seen in Figure 26.

The team looked at other data sets to see if these interpolation methods had a different effect. As seen in Figure 27 and Figure 28, these methods had drastically different effects.

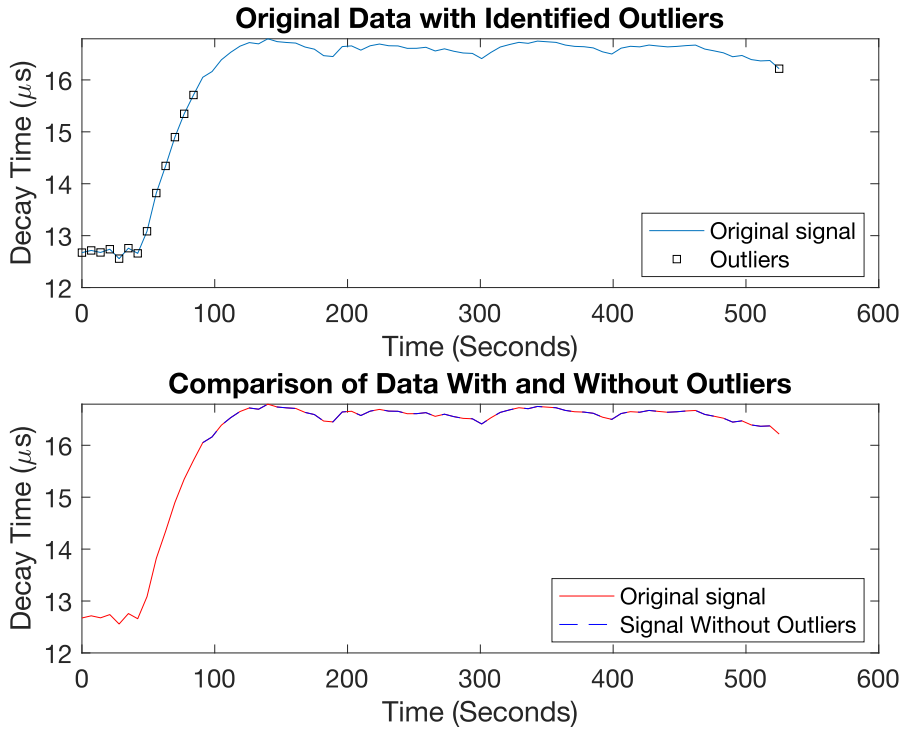

Figure 20: Outlier detection and replacement algorithm successfully applied to data from a previous experiment.

Figure 29 and Figure 30 show how the data differs using the previous and spline interpolation methods. As seen the previous method successfully replaced the outliers, whereas the spline method is not as accurate.

Since the previous and linear interpolation methods had the most consistent and successful results, either method can be used in this outlier detection and replacement algorithm. For the sake of standardizing the process, one method, the previous or linear interpolation method, was used to produce all results.

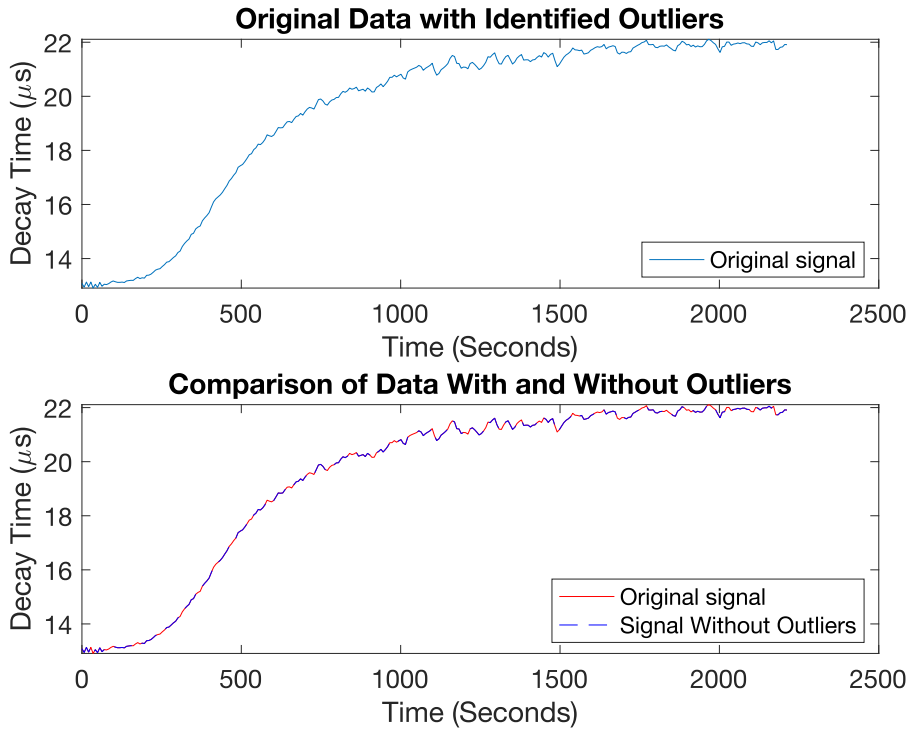

Figure 21: Outlier detection and replacement algorithm successfully applied to data from a previous experiment.

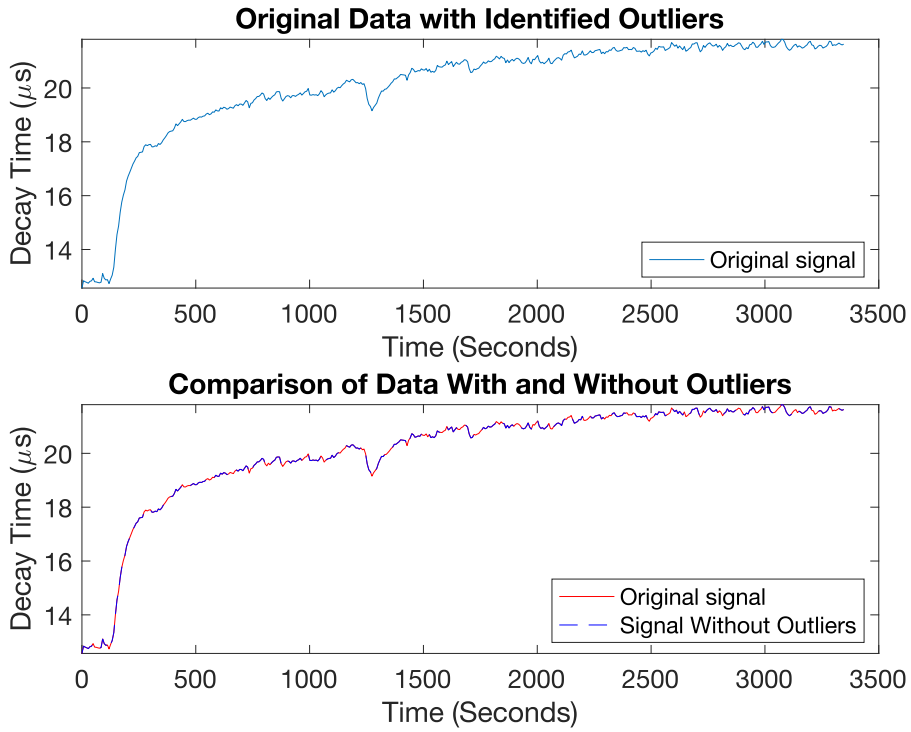

Figure 22: Outlier detection and replacement algorithm successfully applied to data from a previous experiment.

Figure 23: Outlier detection and replacement algorithm successfully applied to data from a previous experiment.

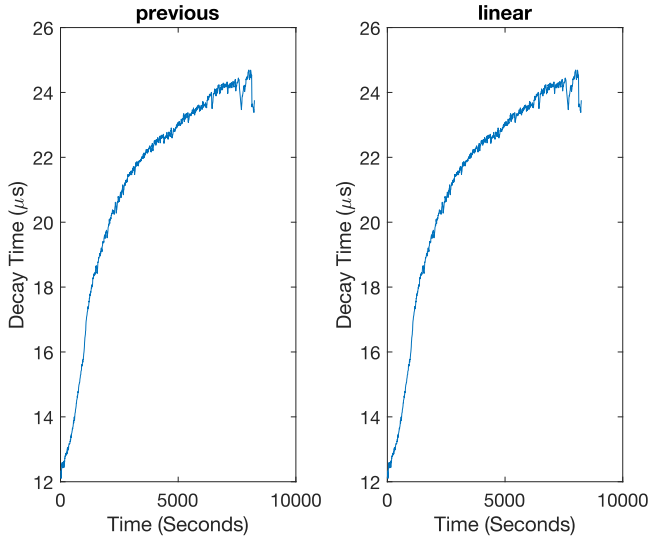

Figure 24: Comparison of previous and linear interpolation methods used to replace outliers from the signal depicted in Figure 11.

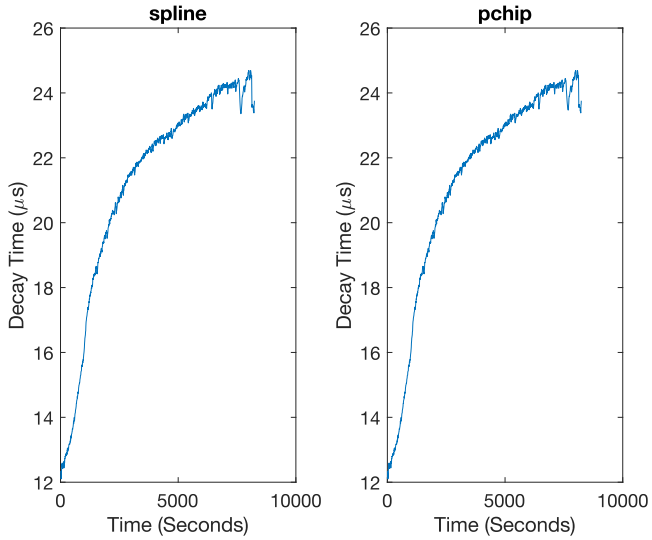

Figure 25: Comparison of spline and pchip interpolation methods used to replace outliers from the signal depicted in Figure 11.

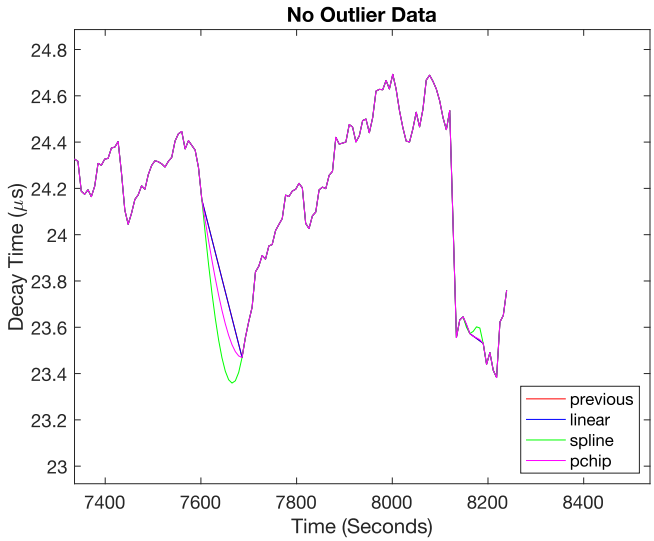

Figure 26: Zoomed in comparison of four interpolation methods used to replace outliers from the signal depicted in Figure 11.

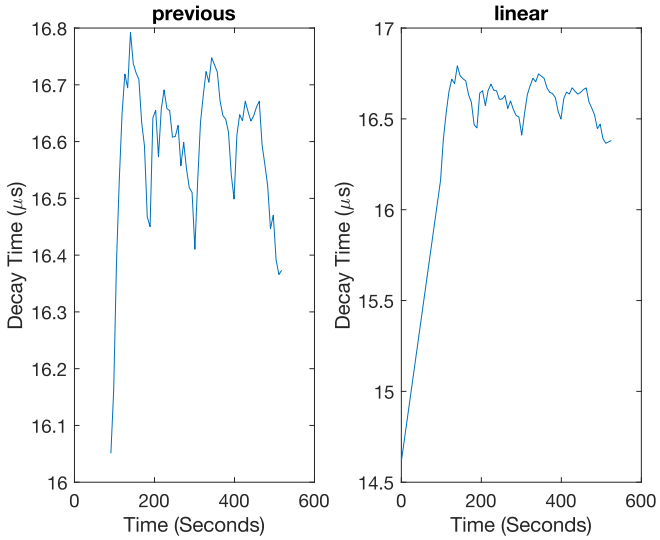

Figure 27: Comparison of previous and linear interpolation methods used to replace outliers from the signal depicted in Figure 20.

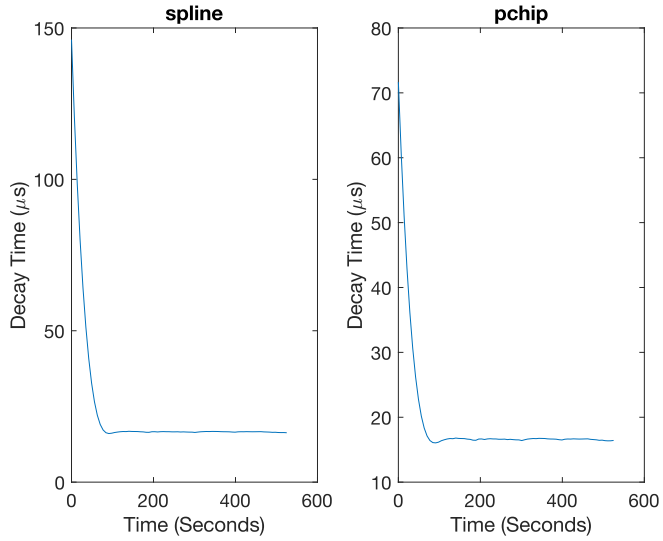

Figure 28: Comparison of spline and pchip interpolation methods used to replace outliers from the signal depicted in Figure 20.

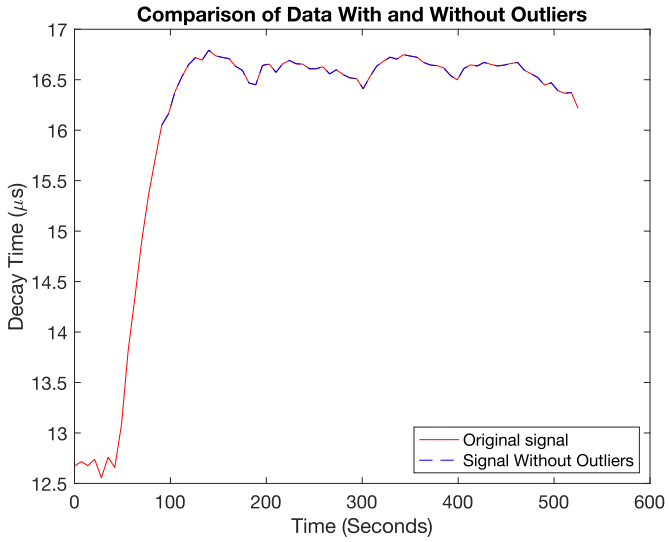

Figure 29: This signal utilizes the previous interpolation method.

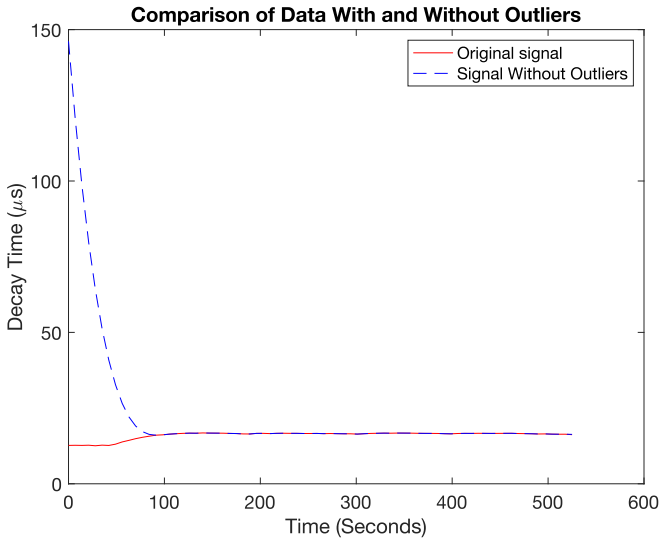

Figure 30: This signal utilizes the spline interpolation method.

6 Hardware Design

The following section will introduce the hardware design of the transcutaneous oxygen sensor prototype. Components will be discussed with respect to their functionality in the device including the power management unit (PMU), sensor head, analog front end (AFE), and microcontroller (MCU).

After testing, the team moved on to miniaturizing the transcutaneous oxygen sensor. By having a smaller overall device size, it is more user-friendly. The size will increase the level of comfort when wearing the device. In an attempt to minimize prototype size, the team opted for a flexible PCB design.

6.1 Block Design

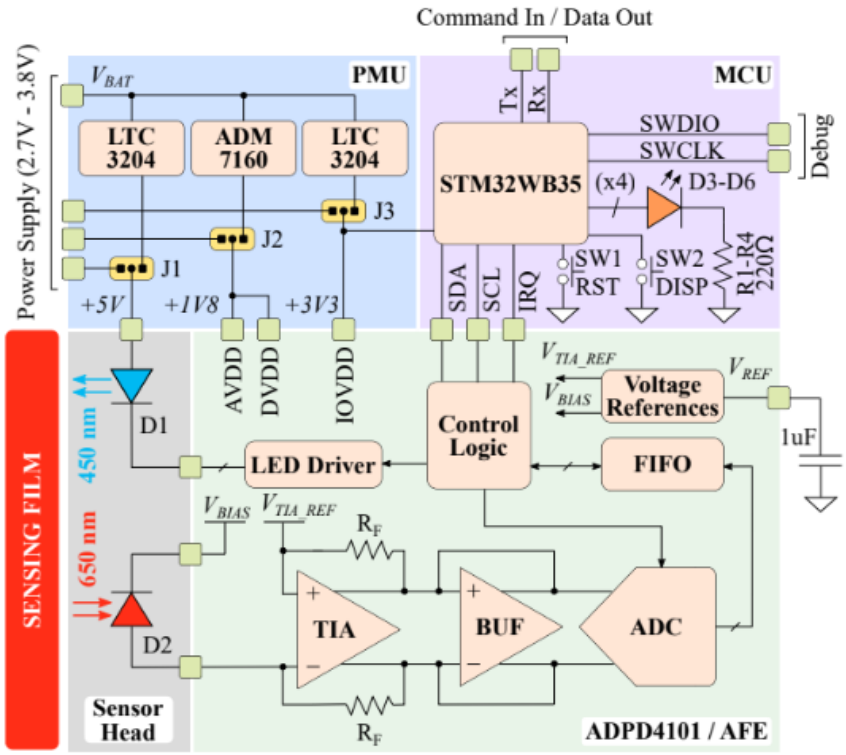

Figure 31: Block diagram of transcutaneous oxygen sensor.

6.1.1 Power Management Unit

The power management unit consists of two boost converters and low dropout regulators (LDO). The boost converters increase the output voltage to a necessary level. While boost converters are highly efficient, they also induce an element of noise. Before connecting to the microcontroller an LDO is used to reduce and regulate the voltage. The LDO offers an advantage as it reduces noise in the system which is critical when used in conjunction with the buck. As the voltage from the original source varies, as the battery drains, the power management system will ensure a consistent voltage is being delivered to the rest of the system. Overall, the PMU produces four varying voltage rails. The 5V power rail to power the device is seen in Figure 32, the 1.8V power rail for the AFE is seen in Figure 35, and there are two separate 3.3V rails, one for the MCU and FLASH integrated circuit (IC) and the other to drive the LEDs are seen in Figure 33 and Figure 34.

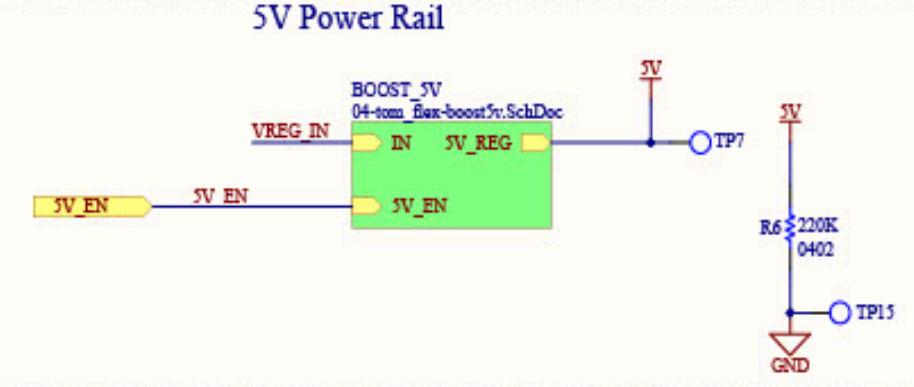

Figure 32: Schematic of 5V power rail.

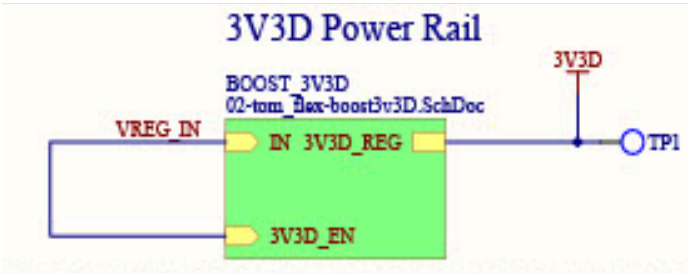

Figure 33: Schematic of 3.3V rail for microcontroller and FLASH IC.

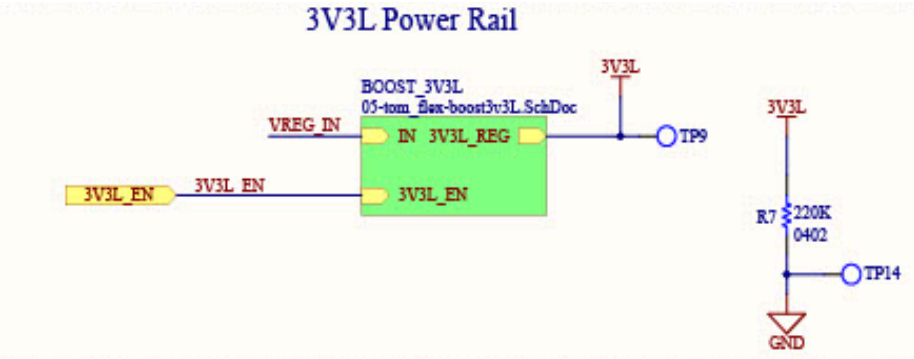

Figure 34: Schematic of 3.3V rail for LEDs.

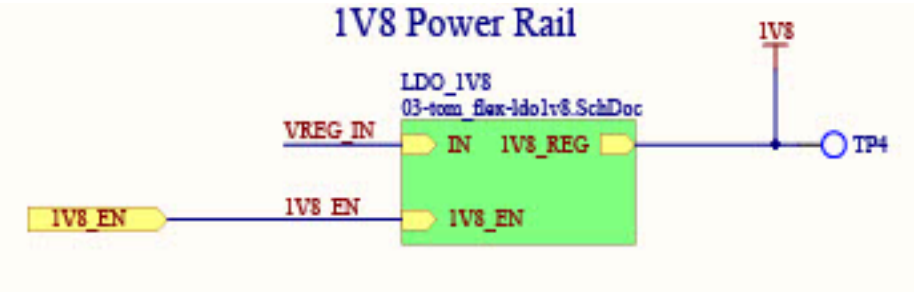

Figure 35: Schematic of 1.8V rail.

External Power Supply The initial PCB board contained an external power supply for testing of the device. During the initial testing of the device, an external power supply was used to ensure constant voltage throughout the board. In the new version of the PCB design, a battery will be used, which is why a coin battery holder is placed on the PCB layout.

Boost Converters The first boost converter is used to boost the input voltage and create the 5V power rail. The second boost converter is placed after the LDO to boost the 1.8V back up to 3.3V One 3.3V power rail is connected to the microcontrollers and FLASH IC, while a secondary 3.3V is connected to the LEDs. The isolation is due to current spikes from the LEDs needing to be separated from the MCU. The schematic of the boost converter is seen in Figure 36.

Low Dropout Regulator The LDO utilized in the design is the ADM7160 [65], which is an ultralow noise linear regulator as seen in Figure 37. In this design, the

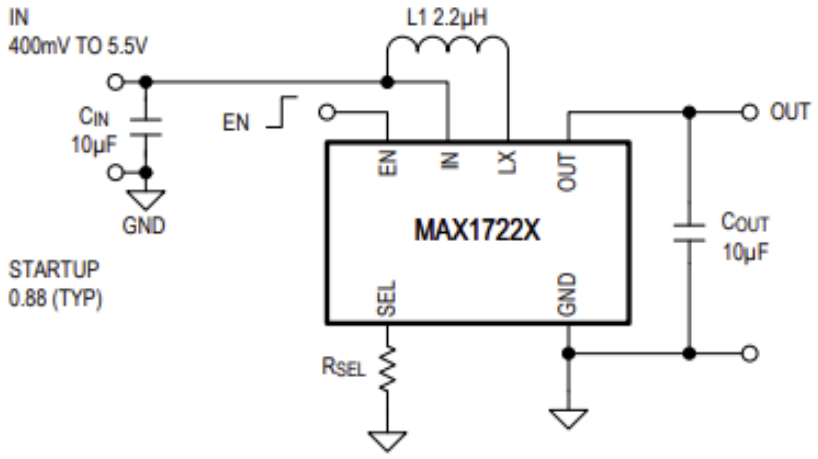

Figure 36: Block diagram of boost converter.

LDO is responsible for dropping the input voltage to 1.8V to produce the analog voltage supply (AVDD) and the digital voltage supply (DVDD).

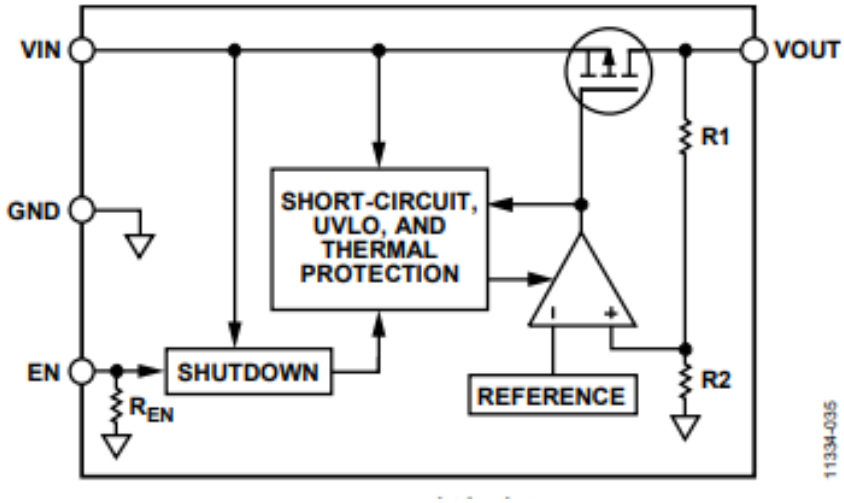

Figure 37: Block diagram of low dropout regulator.

Battery The current implementation of the sensor utilized an external DC power supply or a 3V lithium coin cell battery. The new PCB implementation will have a

coin cell holder for the battery, but the future design aims to have a rechargeable battery or possibly a method for wireless charging. The current implementation of the coin cell battery is shown in Figure 38.

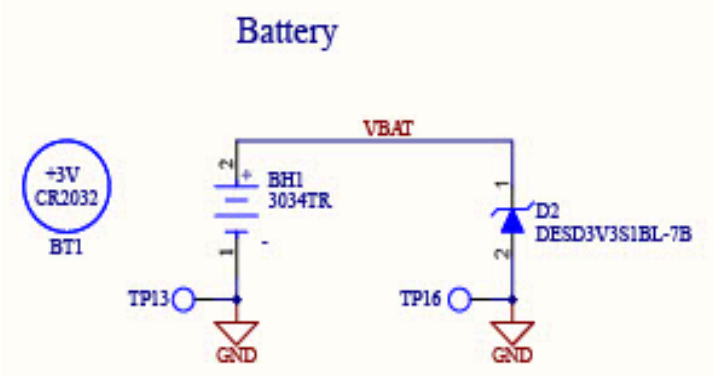

Figure 38: Schematic of battery.

6.1.2 Microcontroller Unit

There were three main functions for the microcontroller unit. First, the MCU (STM32WB35) [66] was used to configure the AFE to drive the LEDs, then receive the digitized luminescent signal from the AFE, and lastly communicate the experimental data with a PC. The MCU utilized is a dual-core system where CPU1 contained the firmware and CPU2 controls the radio frequency (RF) and Bluetooth (BLE) modules. The hardware rest is controlled by switches. These switches are connected to the MCU to enable reset, boot, and control display. I2C protocol is used to communicate between the AFE and the MCU, and universal asynchronous receiver transmitter (UART) protocol is to convey the data to a PC. MCU connections are shown in Figure 39.

Storage and FLASH FLASH provides external memory for storing the data collected. For this design, the stored data contains the calculations for lifetime value. A 3V 32M-bit serial FLASH memory was used for the design as seen in Figure 40. The analog-to-digital converter (ADC) within the AFE writes to a first in first out (FIFO) memory buffer, which acts as short-term storage for data.

Acceleromenter The ADXL367 [67] digital outputs microelectromechanical (MEMS) accelerometer is used in the design as seen in Figure 41. The accelerometer

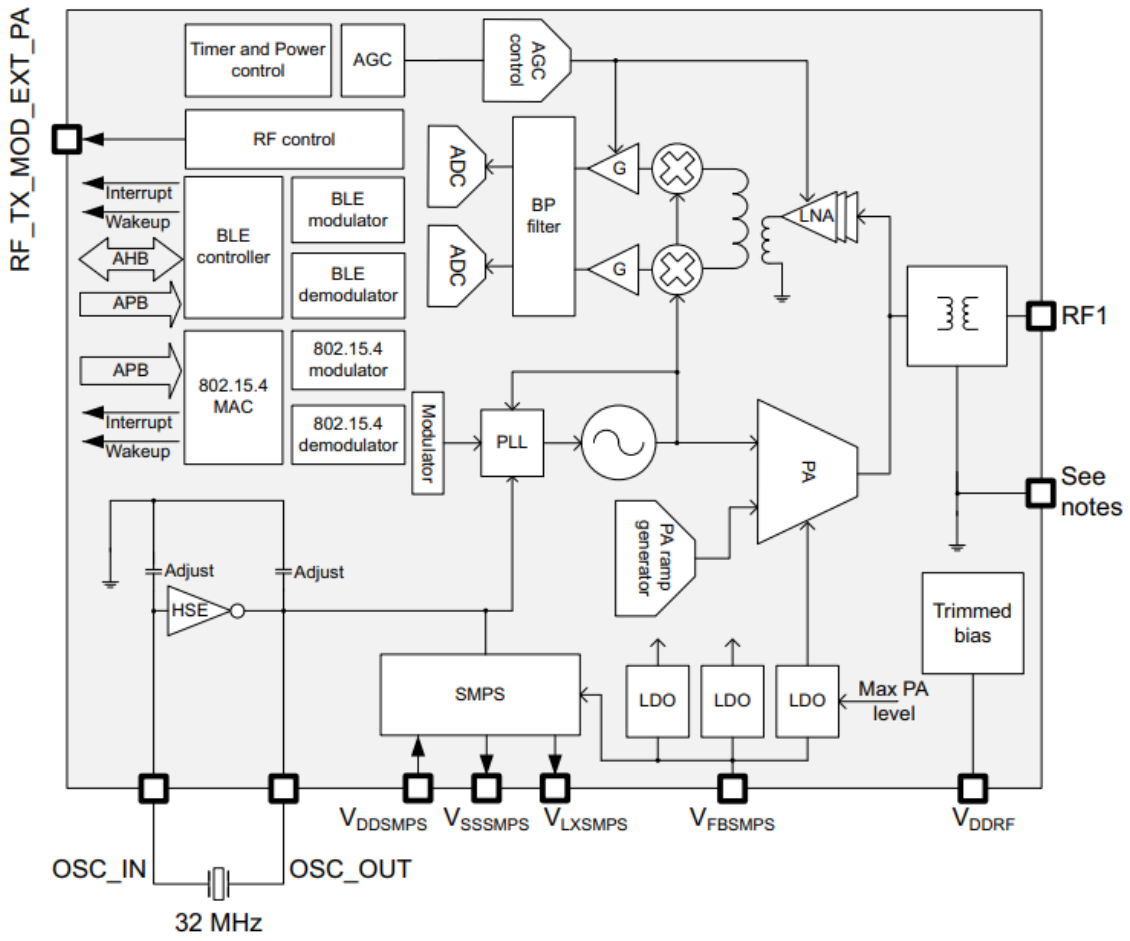

Notes:
- UFQFPN48 and VFQFPN68: V_{SS} through exposed pad, and V_{SSRF} pin must be connected to ground plane
- WLCSP100 and UFBGA129: V_{SSRF} pins must be connected to ground plane

Figure 39: Block diagram of microcontroller.

has low power consumption by sampling the full bandwidth of the sensor rather than aliasing the input signal by undersampling. The schematic of how the accelerometer is connected in the PCB is shown in Figure 42.

6.1.3 Analog Front End

The analog front end device takes in the analog signal being read and converts it into digital data which can be processed by the MCU. The LEDs shine onto the oxygen

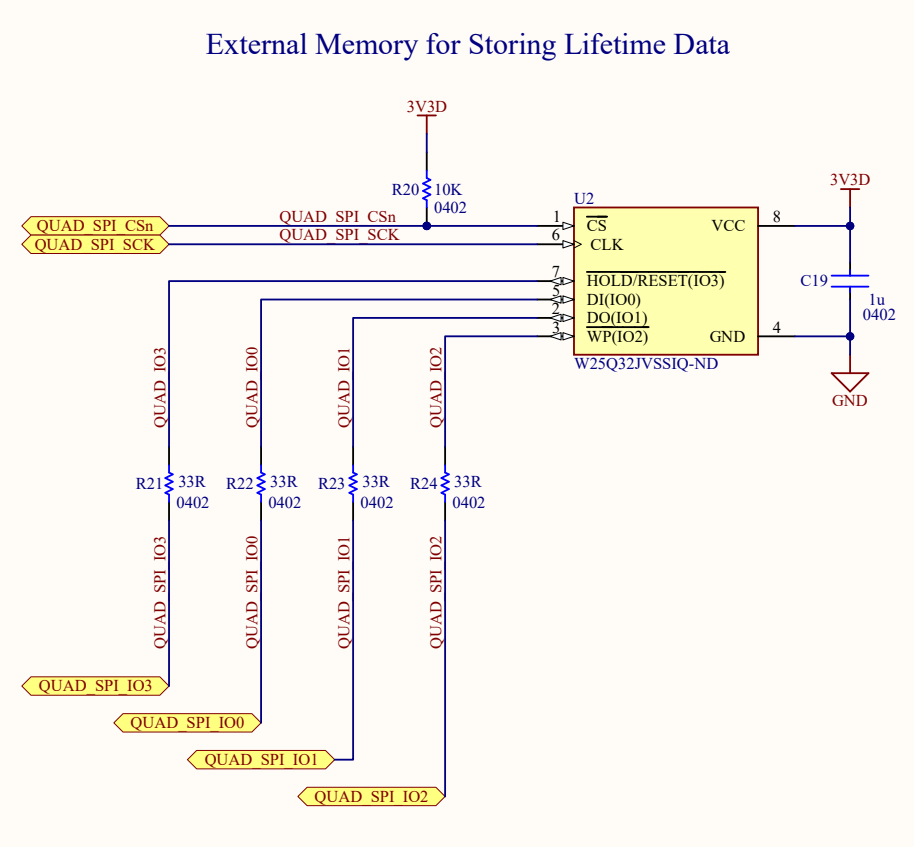

Figure 40: Block diagram of flash IC.

film, and the outputs of the photodiode are read back into the AFE. The intensity of the luminescence reflected is quantified and used as an input to an analog-to-digital converter which is then fed into the input of the MCU.

Integrated Analog Front End The AFE used is the ADPD4101 [7], which is capable of measuring (SpO_2), CO, (CO_2) and specializes in wearable health monitoring as well as home patient monitoring. The AFE consisted of a transimpedence amplifier, a buffer, and an analog-to-digital converter. I2C protocol is used to communicate between the AFE and the MCU. The connections to the AFE are shown in Figure 43.

UART The UART protocol is used to transmit the digitized luminescent data from the MCU to a PC. This transmission of data to an external computer enables

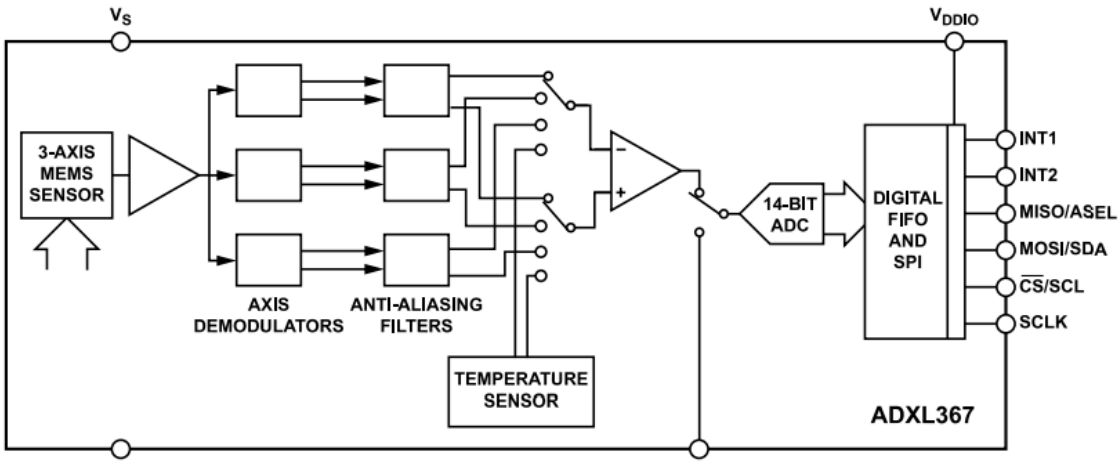

Figure 41: Block diagram of the accelerometer.

the calculation of lifetime decay (Tau) as well as additional signal processing. The UART configuration is shown in Figure 44.

6.1.4 Sensor Head

In the proposed design, there are four major components in the sensor head: pt-porphyrin film, LED, photodiode, and an optical filter.

Temperature Sensor The TMP117[8] is a high-accuracy and low-power digital temperature sensor that was used in the design as seen in Figure 45. The temperature sensor is capable of communicating through the I2C protocol. The proposed design includes the temperature sensor at the bottom of the board that will have a connection to the AFE which is located on the layer above. The connections of the temperature sensor in the PCB are shown in Figure 46.

Pt-Porphyrin Film The Red Eye is a flexible patch that acts as a luminescent sensor that is receptive to oxygen. This portion of the device is directly in contact with the subject's skin. It is the film patch that detects oxygen on the surface of the skin.

LED A LED with a peak wavelength of 450nm, which corresponds to blue light is used in the design of the sensor head. The specific LED utilized is the LXZ1-PR01

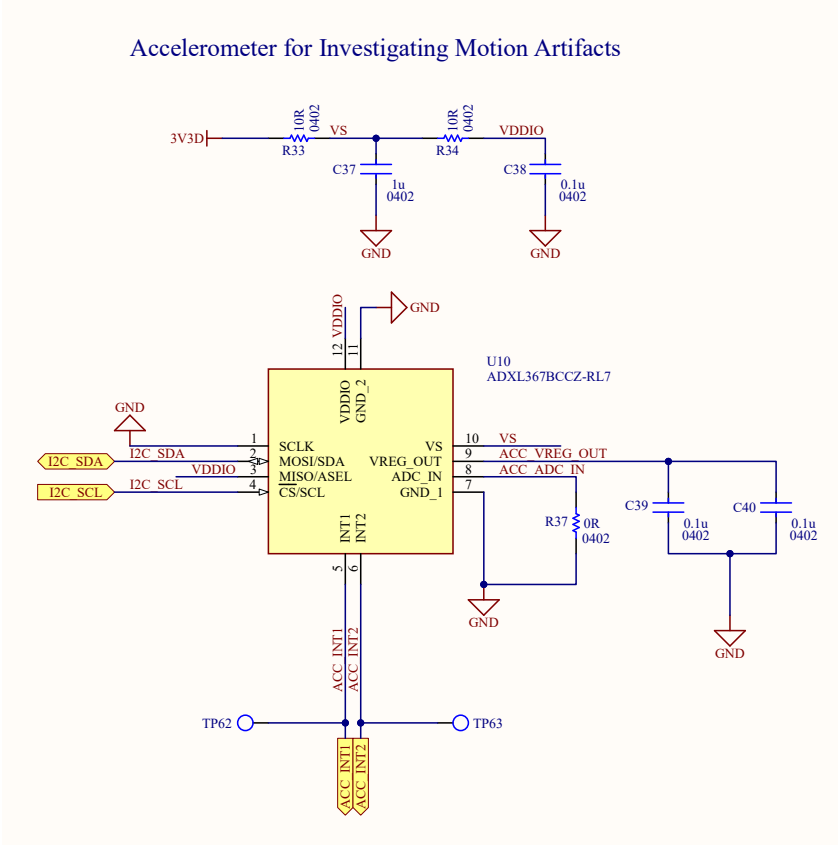

Figure 42: Schematic of the accelerometer.

as seen in Figure 47.

Photodiode A photodiode (PD) was placed in the sensor head to produce a photocurrent, which would then be inputted into the AFE for conversion and processing, this schematic can be seen in Figure 48. The SD019-141-411 is a PD that has an integrated band-pass filter with a peak wavelength of 600nm. This filter only allows for red light to pass.

Optical Filter A long-pass optical filter is used to filter out blue light. The Everix filter functions at 500nm, only passing light above this wavelength. The purpose of this filter is to reduce the effect of blue light on the measurements. This filter is a thin film that is placed above the luminescent sensor patch.

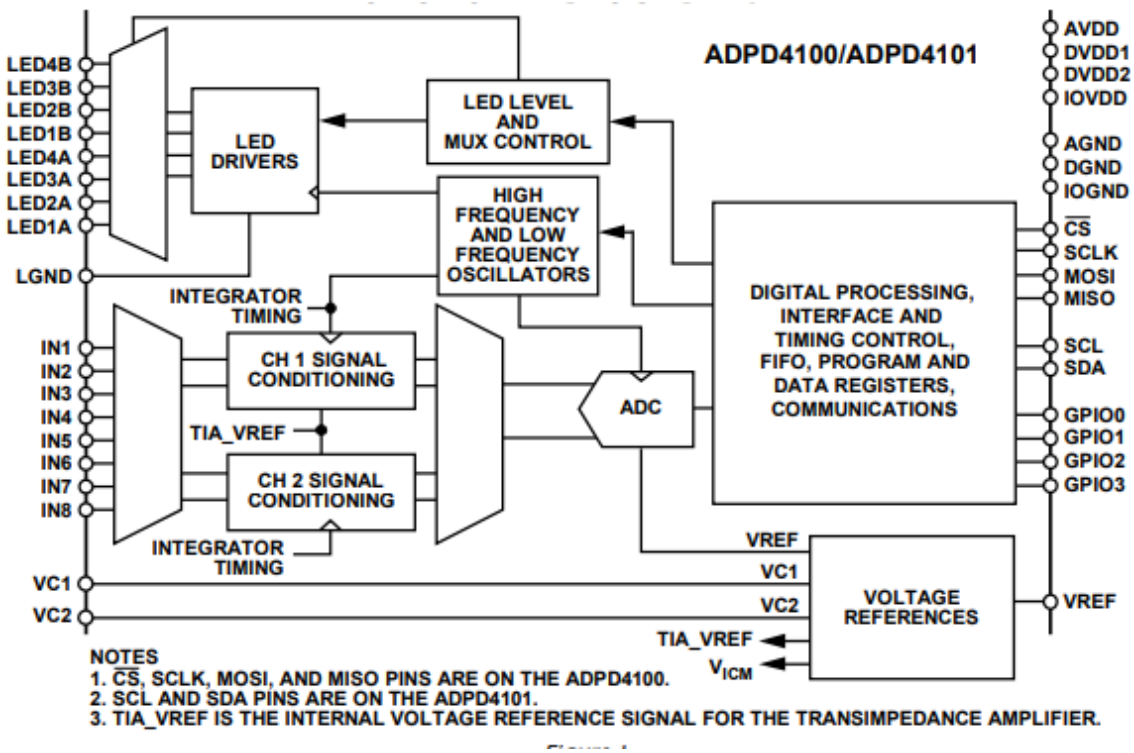

Figure 43: Block diagram of analog front end [7].

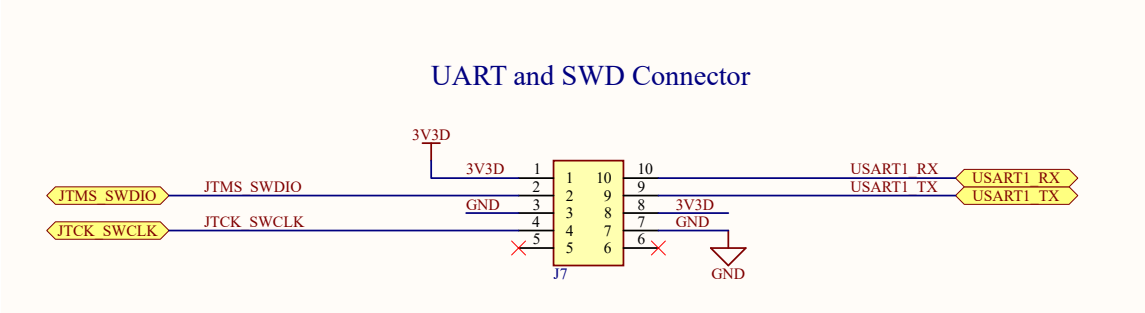

Figure 44: Schematic of UART and SWD.

6.2 Flexible PCB Layout

The team went through multiple iterations until they settled on the most optimal design for the flexible PCB. The initial goal was to produce a miniaturized flexible PCB that contained all of the components of the initial design. Primarily, a one-fold

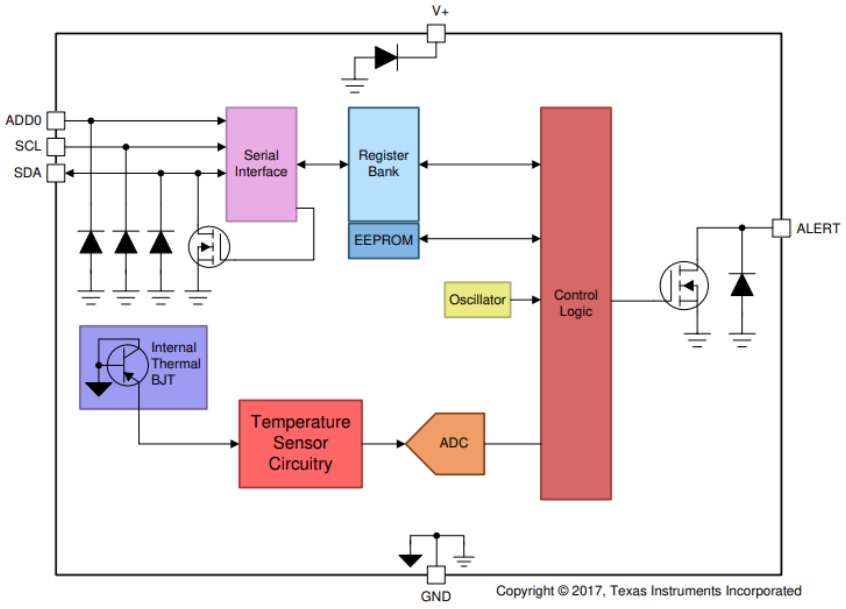

Figure 45: Block diagram of temperature sensor [8].

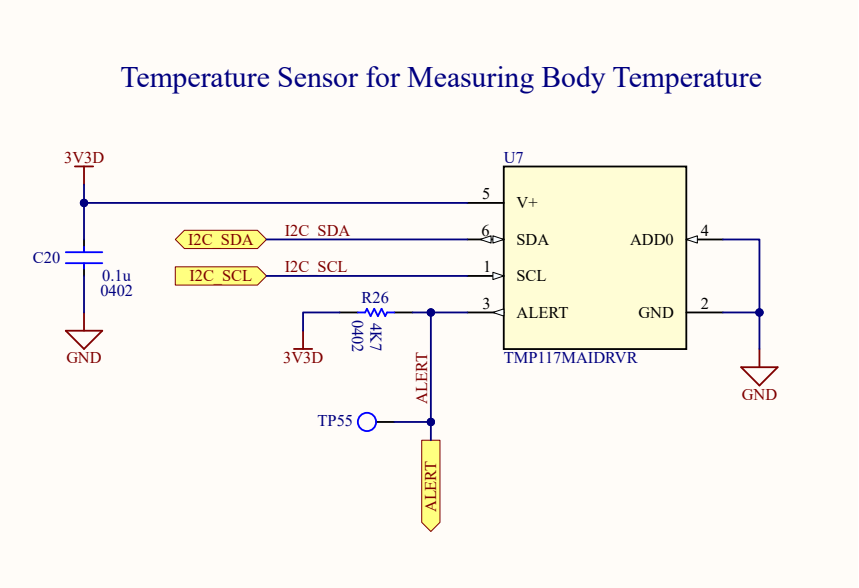

Figure 46: Schematic of temperature sensor.

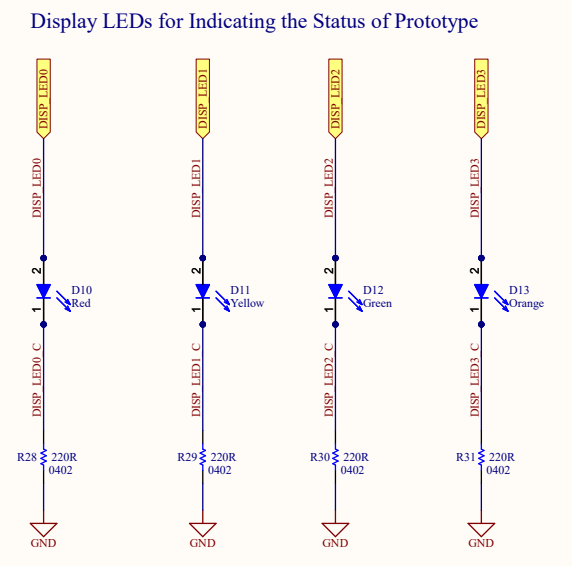

Figure 47: Schematic of LEDs.

and two-layer flexible PCB was proposed, and the team went on to test variously sized PCB designs and then continued to create a two-fold three-layer PCB as well.

6.2.1 Layer Distribution

When designing the two-layer PCB, there were four separate faces available to place components on. The components were divided based on various requirements. The sensor head was placed on the bottom face due to the requirement of needing to be in contact with the subject's skin. Since the AFE was the first stage of processing, it was placed on the face directly above the sensor head. When considering the last two faces, it was clear that the informational LEDs, PMU, and the RF/BLE module would be those that required the least chance of interference, so they were grouped and placed on the topmost face. This left the MCU unit, FLASH, and accelerometer on the face below the PMU. The proposed layout can be seen in Figure 49.

After generating a 40mm x 40mm face for the two-layer board, there was extra space on the PCB. The final 40mm x 40mm designs can be seen in Figures 50, 51, 52. The team went on to optimize space by developing a 30mm x 30mm two-layer board. The final 30mm x 30mm designs can be seen in Figures 53, 54, 55. At this stage, the team considered the possibility of reducing size even more but needed to implement an additional layer. Then the team went on to develop a 20mm x 20mm

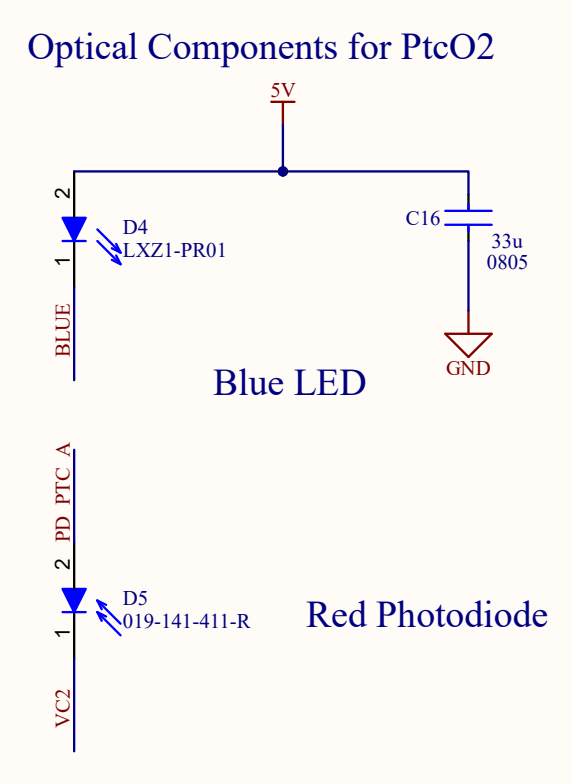

Figure 48: Schematic of optical system.

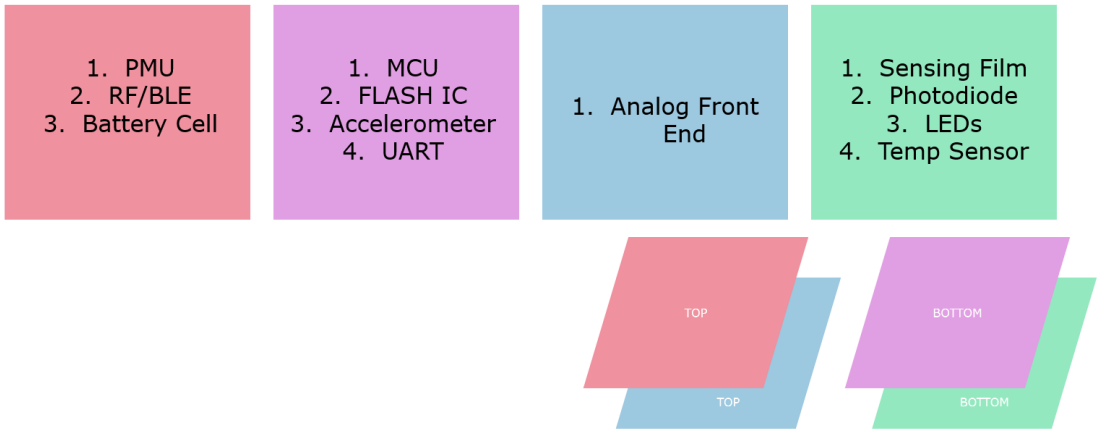

Figure 49: Proposed layout for folded PCB.

three-layer board. The final 20mm x 20mm designs can be seen in Figures 56, 57, 58.

When designing the three-layer PCB, the component breakdown had to be adjusted. The team left the bottom face to include the sensor head, and the face directly above it to include the AFE. At this point, the team had to isolate which components needed space at the topmost layer, which would be the LEDs, RF/BLE, and battery cell. These three components were placed on the topmost face, and directly below it was the PMU for shorter connections. The middle layer contained the MCU on the top face and the FLASH, accelerometer, and additional switch on the bottom face.

6.2.2 Optimizing Space and Layout

There were three iterations of the flexible PCB. The first iteration was the 40mm x 40mm two-layer PCB. The main issue with this design was the empty space at the bottom layer. This left enough room to develop a smaller iteration.

The team then tried to follow the same design but on a smaller scale of 30mm x 30mm. The main issue with this design was that the AFE and sensor head did not require the full board space allotted. Therefore the space could be used more effectively. Additionally, the distribution of components was uneven. While the faces with the AFE and sensor head had excess room, the MCU and PMU sides were crowded with components. As a result, the battery cell holder did not entirely fit this design. The team wanted to try to fit everything in a smaller space, but this

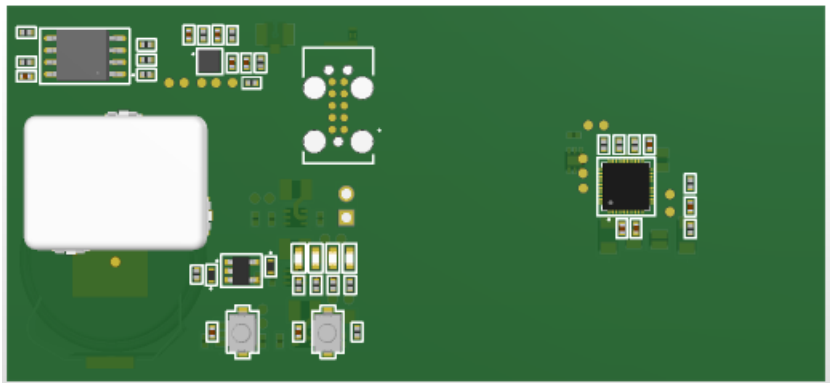

Figure 50: Unfolded bottom layout of 40mm PCB.

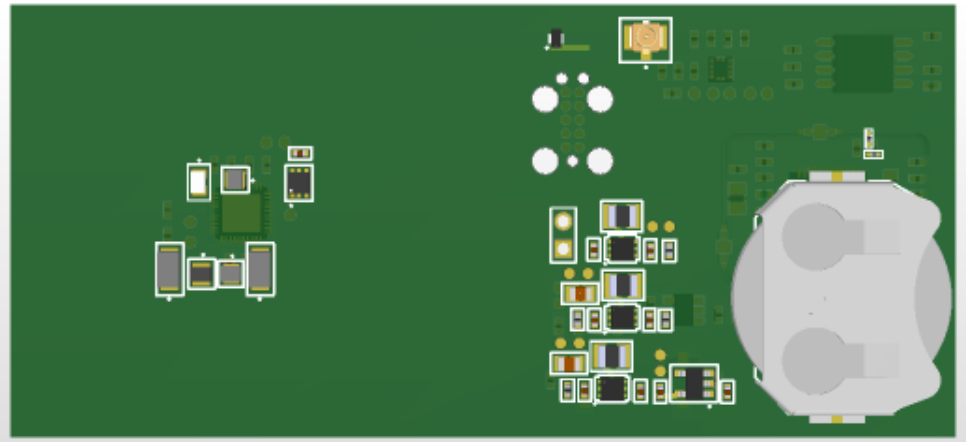

Figure 51: Unfolded top layout of 40mm PCB.

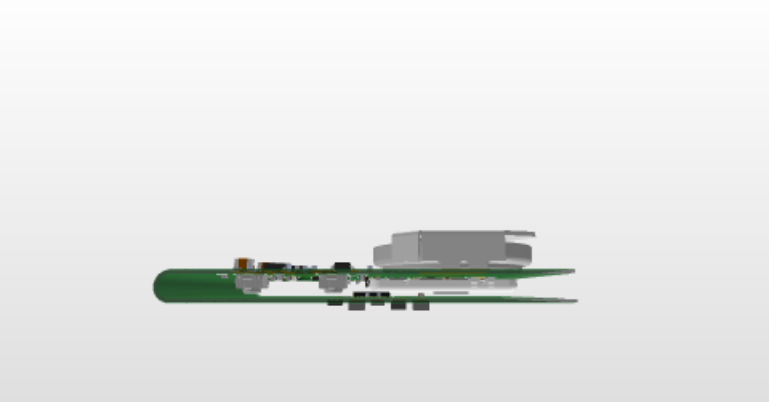

Figure 52: Folded layout of 40mm PCB.

would require another layer to the PCB.

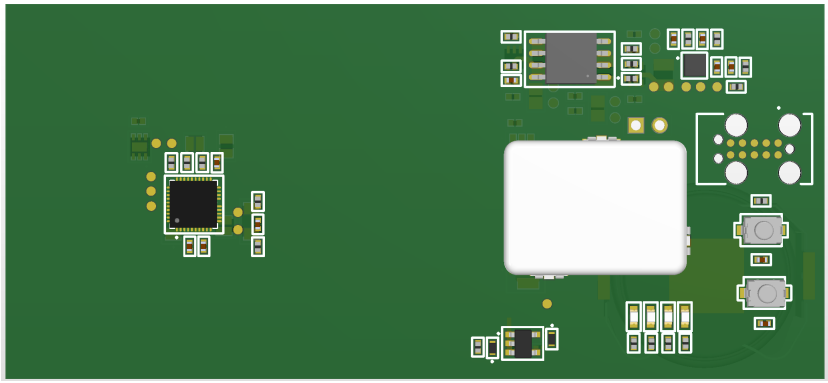

Figure 53: Unfolded bottom layout of 30mm PCB.

Finally, the team developed a design where the faces were 20mm x 20mm but there were three layers instead of two. The PCB design is now primarily dependent on the packaging constraints of the device and future battery modifications. The largest component on the PCB is the coin cell battery holder. If this component can be removed or modified to incorporate power using a less bulky component the overall size of the PCB could be even further reduced.

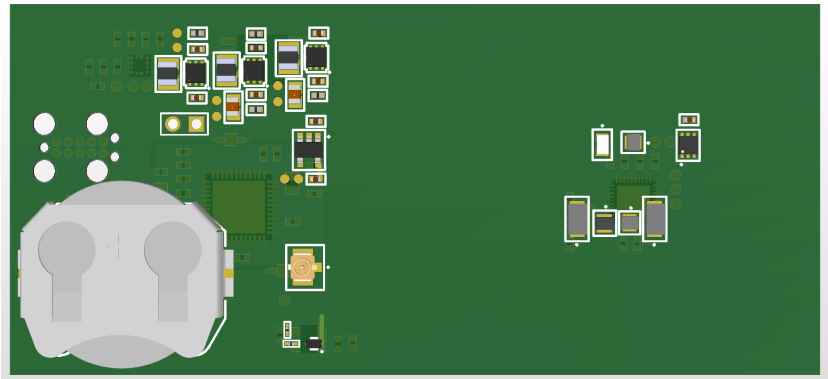

Figure 54: Unfolded top layout of 30mm PCB.

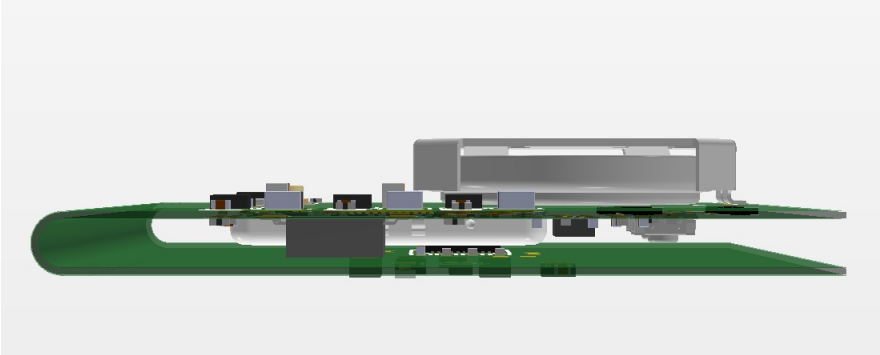

Figure 55: Folded layout of 30mm PCB.

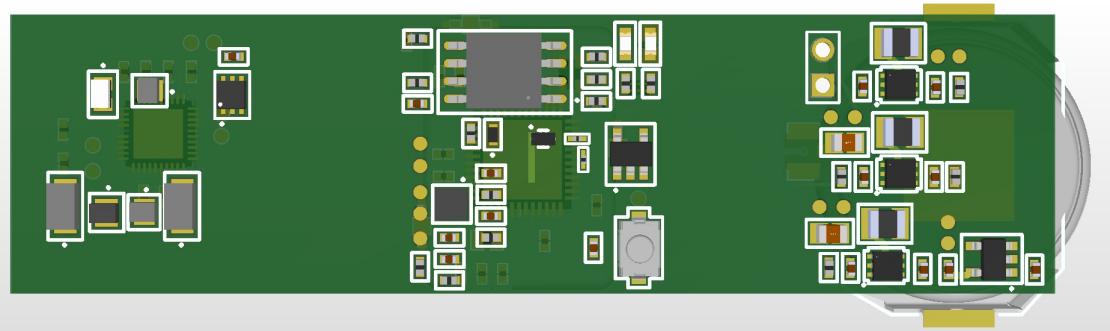

Figure 56: Unfolded bottom layout of 20mm PCB.

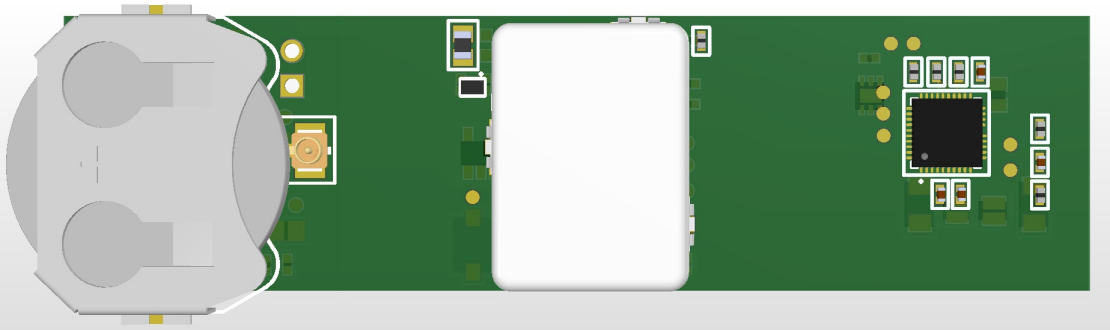

Figure 57: Unfolded top layout of 20mm PCB.

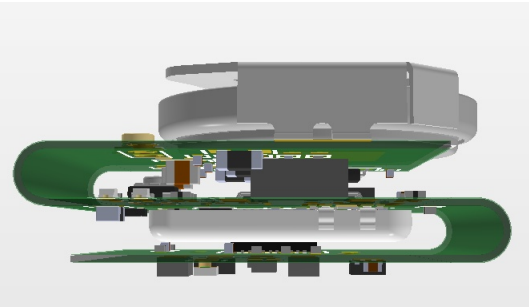

Figure 58: Folded layout of 20mm PCB.

7 Suggestions

In this section, we outline future modifications to the transcutaneous oxygen sensor. Ultimately, the objective of sensor development is to improve the capabilities of the current prototype and work toward making the sensors suitable for practical use in remote health monitoring.

The next immediate step will be finalizing the redesign of the flexible PCB. Any additional decrease in size will benefit the usability of the device for remote monitoring, as patients should ideally be uninhibited by the device's size. The flexible PCB will need to be encapsulated into a packaging attachment for patient use. Testing will also need to be conducted using the flexible version to ensure the functionality of the original device has been retained.

There are also potential improvements regarding data transmission. Currently, the prototype is hardwired and relies on connections to both the power source and CPU for data collection. The sensor has components to make it capable of wireless transmission and Bluetooth in the future. In order to become a feasible remote device, these technological developments are critical. Future uses of the device may require data transmission from a patient to a doctor who can continuously monitor the subject's vitals.

It is important that all components of the sensor are able to be decontaminated to remove microbials on the surface of the device. Research has been conducted that is currently in the beginning phases and has suggested promising results. Important parts of the decontamination process include mitigating risk to the integrity of the sensor. It is important not to compromise the film accuracy and the sensor's electrical components. The film data sheet indicates that the film can be in contact with ethanol and not risk reduction in accuracy. Ethanol as a sterilizing agent has been used effectively in healthcare [52]. Along with the film, research suggests ethanol is an effective method of cleaning electronics. Through the use of pure-ethanol, electronics can be decontaminated with minimal risk to electrical component damage [53].

Further testing will be required to determine how to sterilize the film needed for repeated device use. Various cleaning techniques can be tested, and the impact of the film quality should be analyzed over a series of varying time intervals to observe any potential changes.

Other methods of decontamination that are compatible with electronics include Ultraviolet C (UVC). No research has been conducted on its impact on the film however, UVC has promising results for electronic decontamination. In a study conducted, 87% of the surfaces had a reduction in microbes [54]. It was also determined that the amount of decontamination was dependent on the exposure time to the

UVC [54].

Methods of decontamination that have been studied for current market devices include neutral electrolyzed water. In a study to prevent infection while using a transcutaneous oxygen monitor, it was found that exposure to electrolyzed water removed microbes on the surface of the sensor [55]. While this research is still in the early stages, it is important to determine methods of decontamination and the research has indicated multiple methods to be further investigated.

Testing was conducted using constant pressure without any movement of the subject. For the sensor to become viable for remote patient monitoring, the device needs to be able to withstand movement. An accelerometer has been added to the PCB, but the functionality must be implemented and tested. The accelerometer will be able to track the movement of the subject. By tracking motion and understanding how movement impacts the accuracy of the sensor, the readings can be calibrated. Data processing can be implemented to account for any potential physical disturbances caused to the oxygen measurements. With this additional functionality, the packaging of the device must be modified to adhere directly to the skin.

In regards to packaging, further developments can be made to improve the usability of the device. An ideal solution would involve removable sections of the device. The remote monitoring device could be split up into three different parts, one containing the battery, another containing the PCB core, and the last containing the LEDs and film which makes contact with the skin. The battery could be improved in the future to become rechargeable thus reducing the number of disposable components the device uses. The film section will either need to be disposable or a method must be found to sanitize the film. Testing needs to be done to determine the exact lifetime of the film and experiments on how possible sanitization efforts would impact the sensor readings.

8 Conclusion

The goal of this project was to evaluate the viability of the transcutaneous oxygen sensor within the medical field. Various body locations were tested to evaluate the optimal placement of the sensor. Four subjects were assessed to verify the prototype's accuracy across a diverse patient range. While the lifetime values and subsequent settling times of each body location differed, the device produced consistent and accurate readings across multiple subjects. Ultimately, all locations have the potential to produce viable data and the optimal location will depend of the specific user application. Future modifications have been outlined to help the transition of the prototype into an operable product for remote patient care. The beginning steps include improving the data processing procedure and modifying the PCB design to decrease the overall size of the device.

References

[1] S. Hobson, A. Leonardi, C. Murphy, V. Rohera, V. Vakhter, B. Kahraman, U. Guler, G. Bu, F. Foroozan, and L. Rhein, "Optimizing transcutaneous oxygen measurement site on humans," in *2032 Engineering in Medicine and Biology Society (EMBC)*. IEEE, 2023, pp. 1–4.

[2] S. Hobson, A. Leonardi, C. Murphy, and V. Rohera, "Outlier detection and removal signal processing for wearable transcutaneous oxygen sensor," in *2032 MIT Undergraduate Research Technology Conference (MIT URTC)*. IEEE, 2023, pp. 1–4.

[3] I. Costanzo, D. Sen, and U. Guler, "An integrated readout circuit for a transcutaneous oxygen sensing wearable device," in *2020 IEEE Custom Integrated Circuits Conference (CICC)*. IEEE, 2020, pp. 1–4.

[4] I. Costanzo, D. Sen, J. McNeill, and U. Guler, "A nonuniform sampling lifetime estimation technique for luminescent oxygen measurements," in *ESSCIRC 2022-IEEE 48th European Solid State Circuits Conference (ESSCIRC)*. IEEE, 2022, pp. 413–416.

[5] "The principles of transcutaneous monitoring." [Online]. Available: https://www.radiometeramerica.com/en-us/products/transcutaneous-monitoring/the-principles-of-transcutaneous-monitoring

[6] F. Gul, O. F. Boran, and R. Arslantas, "Microcirculation and hyperbaric oxygen treatment," *Hyperbaric Oxygen Treatment in Research and Clinical Practice–Mechanisms of Action in Focus. IntechOpen*, pp. 47–66, 2018.

[7] *Analog Devices Inc.* ADPD4101: product datasheet and information, [Online]. Available: https://www.analog.com/en/products/adpd4101.html. [Accessed Dec.5, 2022].

[8] *Analog Devices Inc.* TMP117: product datasheet and information, [Online]. Available: https://www.ti.com/product/TMP117?utm_source=google&utm_medium=cpc&utm_campaign=asc-null-null-gpn_en-cpc-pf-google-wwe&utm_content=tmp117&ds_k=TMP117&dcm=yes&gclid=Cj0KCQjwla-hBhD7ARIsAM9tQKunWZ_cXwaJS-TrPKlP1cmb8u6TFw66LSd_qf2SP1qVwTx4VwLyJ4kaAvg4EALw_wcB&gclsrc=aw.ds. [Accessed Apr.4, 2023].

[9] J. E. Brinkman, F. Toro, and S. Sharma, "Physiology, respiratory drive," in *StatPearls [Internet]*. StatPearls Publishing, 2021.

[10] A. Nicolò, C. Massaroni, E. Schena, and M. Sacchetti, "The importance of respiratory rate monitoring: From healthcare to sport and exercise," *Sensors*, vol. 20, no. 21, p. 6396, 2020.

[11] "Who coronavirus (covid-19) dashboard." [Online]. Available: https://covid19.who.int/

[12] "The top 10 causes of death." [Online]. Available: https://www.who.int/news-room/fact-sheets/detail/the-top-10-causes-of-death

[13] W. Ni, X. Yang, D. Yang, J. Bao, R. Li, Y. Xiao, C. Hou, H. Wang, J. Liu, D. Yang *et al.*, "Role of angiotensin-converting enzyme 2 (ace2) in covid-19," *Critical Care*, vol. 24, no. 1, pp. 1–10, 2020.

[14] U. Guler, I. Costanzo, and D. Sen, "Emerging blood gas monitors: How they can help with covid-19," *IEEE Solid-State Circuits Magazine*, vol. 12, no. 4, pp. 33–47, 2020.

[15] "Covid-19 and the lungs." [Online]. Available: https://www.nhlbi.nih.gov/covid/lungs

[16] "How do lungs work." [Online]. Available: https://www.ncbi.nlm.nih.gov/books/NBK401240/

[17] "Physiology of circulation." [Online]. Available: https://training.seer.cancer.gov/anatomy/cardiovascular/blood/physiology.html

[18] A. J. Williams, "Assessing and interpreting arterial blood gases and acid-base balance," *Bmj*, vol. 317, no. 7167, pp. 1213–1216, 1998.

[19] "Arterial blood gas (abg): What it is, purpose, procedure amp; levels." [Online]. Available: https://my.clevelandclinic.org/health/diagnostics/22409-arterial-blood-gas-abg

[20] M. M. Kmiec, H. Hou, M. Lakshmi Kuppusamy, T. M. Drews, A. M. Prabhat, S. V. Petryakov, E. Demidenko, P. E. Schaner, J. C. Buckey, A. Blank *et al.*, "Transcutaneous oxygen measurement in humans using a paramagnetic skin adhesive film," *Magnetic resonance in medicine*, vol. 81, no. 2, pp. 781–794, 2019.

[21] K. D. Torp, P. Modi, and L. V. Simon, "Pulse oximetry," in *StatPearls [Internet]*. StatPearls Publishing, 2022.

[22] E. D. Chan, M. M. Chan, and M. M. Chan, "Pulse oximetry: understanding its basic principles facilitates appreciation of its limitations," *Respiratory medicine*, vol. 107, no. 6, pp. 789–799, 2013.

[23] B. Carter, D. Wiwczaruk, M. Hochmann, A. Osborne, and R. Henning, "Performance of transcutaneous pco2 and pulse oximetry monitors in newborns and infants after cardiac surgery," *Anaesthesia and intensive care*, vol. 29, no. 3, pp. 260–265, 2001.

[24] A. Madan, "Correlation between the levels of spo2 and pao2," *Lung India*, vol. 34, no. 3, pp. 307–308, 2017.

[25] I. R. McPhail, L. T. Cooper, D. O. Hodge, M. E. Cabanela, and T. W. Rooke, "Transcutaneous partial pressure of oxygen after surgical wounds," *Vascular Medicine*, vol. 9, no. 2, pp. 125–127, 2004.

[26] B. B. Hafen and S. Sharma, "Oxygen saturation," 2018.

[27] D. Sen et al., "Contemporary and nascent techniques for monitoring of oxygenation as a vital sign," in *2020 IEEE 63rd International Midwest Symposium on Circuits and Systems (MWSCAS)*. IEEE, 2020, pp. 647–650.

[28] I. Costanzo, D. Sen, and U. Guler, "A prototype towards a transcutaneous oxygen sensing wearable," in *2019 IEEE Biomedical Circuits and Systems Conference (BioCAS)*. IEEE, 2019, pp. 1–4.

[29] C. Massaroni, A. Nicolò, E. Schena, and M. Sacchetti, "Remote respiratory monitoring in the time of covid-19," *Frontiers in physiology*, vol. 11, p. 635, 2020.

[30] A. Kral, F. Aplin, and H. Maier, "Chapter10 - advanced concepts physical chemistry: Electrodes and electrolytes," in *Prostheses for the Brain*, A. Kral, F. Aplin, and H. Maier, Eds. Academic Press, pp. 167–208. [Online]. Available: https://www.sciencedirect.com/science/article/pii/B9780128188927000146

[31] I. Costanzo et al., "A noninvasive miniaturized transcutaneous oxygen monitor," *IEEE Transactions on Biomedical Circuits and Systems*, vol. 15, no. 3, pp. 474–485, Jun. 2021.

[32] M. Miniaev, M. Belyakova, N. Kostiuk, D. Leshchenko, and T. Fedotova, "Non-obvious problems in clark electrode application at elevated temperature and ways of their elimination," *Journal of Analytical Methods in Chemistry*, vol. 2013, 2013.

[33] B. Kahraman et al., "A miniaturized prototype for continuous noninvasive transcutaneous oxygen monitoring," *2022 IEEE Biomedical Circuits and Systems Conference (BioCAS)*, pp. 486–490, 2022.

[34] R. N. Pittman, "The circulatory system and oxygen transport," in *Regulation of Tissue Oxygenation*. Morgan & Claypool Life Sciences, 2011.

[35] I. D. Stephen, V. Coetzee, M. Law Smith, and D. I. Perrett, "Skin blood perfusion and oxygenation colour affect perceived human health," *PloS one*, vol. 4, no. 4, p. e5083, 2009.

[36] J. King and D. R. Lowery, "Physiology, cardiac output," 2017.

[37] "International online medical council (iomc)." [Online]. Available: https://www.iomcworld.org/medical-journals/vasoconstriction-37490.html

[38] "Vascular disease." [Online]. Available: https://medlineplus.gov/vasculardiseases.html

[39] N. Charkoudian, "Mechanisms and modifiers of reflex induced cutaneous vasodilation and vasoconstriction in humans," *Journal of applied physiology*, vol. 109, no. 4, pp. 1221–1228, 2010.

[40] "Vasodilators: Types and side effects." [Online]. Available: https://my.clevelandclinic.org/health/drugs/23207-vasodilators

[41] U. K. Franzeck et al., "Transcutaneous oxygen tension and capillary morphologic characteristics and density in patients with chronic venous incompetence." *Circulation*, vol. 70, no. 5, pp. 806–811, 1984.

[42] B. J. McGuire and T. Secomb, "Estimation of capillary density in human skeletal muscle based on maximal oxygen consumption rates," *American Journal of Physiology-Heart and Circulatory Physiology*, vol. 285, no. 6, pp. H2382–H2391, 2003.

[43] R. Samsel et al., "Oxygen delivery to tissues," *European Respiratory Journal*, vol. 4, no. 10, pp. 1258–1267, 1991.

[44] G. Basaranoglu et al., "Comparison of SpO_2 values from different fingers of the hands," *Springerplus*, vol. 4, no. 1, p. 561, 2015.

[45] L. Gliemann, "Training for skeletal muscle capillarization: a janus-faced role of exercise intensity?" *European journal of applied physiology*, vol. 116, no. 8, pp. 1443–1444, 2016.

[46] S. P. Philimon, A. K. Huong, W. Hafizah, P. Ong, and X. T. Ngu, "Optical investigation of variability in body region dependent transcutaneous oxygen saturation," in *IOP Conference Series: Materials Science and Engineering*, vol. 160, no. 1. IOP Publishing, 2016, p. 012089.

[47] T. Nishiyama, S. Nakamura, and K. Yamashita, "Comparison of the transcutaneous oxygen and carbon dioxide tension in different electrode locations during general anaesthesia," *European journal of anaesthesiology*, vol. 23, no. 12, pp. 1049–1054, 2006.

[48] D. F. Blake, D. A. Young, and L. H. Brown, "Transcutaneous oximetry: variability in normal values for the upper and lower limb," *Diving and hyperbaric medicine*, vol. 48, no. 1, p. 2, 2018.

[49] R. D. Restrepo, K. R. Hirst, L. Wittnebel, and R. Wettstein, "Aarc clinical practice guideline: transcutaneous monitoring of carbon dioxide and oxygen: 2012," *Respiratory care*, vol. 57, no. 11, pp. 1955–1962, 2012.

[50] A. Leonardi, C. Murphy, S. Hobson, V. Rohera, V. Vakhter, B. Kahraman, G. Bu, F. Foroozan, L. Rhein, and U. Guler, "Optimizing transcutaneous oxygen measurement sites on humans," *EMBC*, 2023.

[51] "Peel-and-stick redeye oxygen sensing patches." [Online]. Available: https://www.oceaninsight.com/products/sampling-accessories/sensors/oxygen/oxygen-patches/

[52] F. Mathew and A. Goyal, "Ethanol," 2020.

[53] P. by Lab Pro, "Ethyl alcohol vs. isopropyl alcohol for cleaning electronics in the lab." [Online]. Available: https://labproinc.com/blogs/chemicals-and-solvents/ethyl-alcohol-vs-isopropyl-alcohol-for-cleaning-electronics-in-the-lab

[54] S. Cremers-Pijpers, C. van Rossum, M. Dautzenberg, H. Wertheim, A. Tostmann, and J. Hopman, "Disinfecting handheld electronic devices with uv-c in

a healthcare setting," *Infection Prevention in Practice*, vol. 3, no. 2, p. 100133, 2021.

[55] S. J. Dancer, J. Mallon, R. Murphy, and C. Murch, "In-use effect of electrolysed water on transcutaneous oxygen sensors," *Healthcare infection*, vol. 20, no. 3-4, pp. 141–144, 2015.

[56] B. Linke, "Sterilization methods and their impact on medical devices containing electronics," *EE Times*, vol. 8, 2011.

[57] "Filter outliers using hampel identifier." [Online]. Available: https://www.mathworks.com/help/dsp/ref/hampelfilter.html

[58] "Outlier removal using hampel identifier." [Online]. Available: https://www.mathworks.com/help/signal/ref/hampel.html

[59] "Detect and remove outliers in data." [Online]. Available: https://www.mathworks.com/help/matlab/ref/rmoutliers.html#d124e1317148

[60] "Detect and replace outliers in data." [Online]. Available: https://www.mathworks.com/help/matlab/ref/filloutliers.html#d124e462722

[61] "1-d median filtering." [Online]. Available: https://www.mathworks.com/help/signal/ref/medfilt1.html

[62] "1-d digital filter." [Online]. Available: https://www.mathworks.com/help/matlab/ref/filter.html

[63] "Filter data." [Online]. Available: https://www.mathworks.com/help/matlab/data_analysis/filtering-data.html

[64] "Fill missing entries." [Online]. Available: https://www.mathworks.com/help/matlab/ref/fillmissing.html

[65] *Analog Devices Inc.* ADM7160: product datasheet and information, [Online]. Available: https://www.analog.com/en/products/adm7160.html. [Accessed Apr.4, 2023].

[66] *STMicroelectronics* STM32WB35/55xx microcontroller: product datasheet, [Online]. Available: https://www.st.com/resource/en/datasheet/stm32wb55cc.pdf. [Accessed Apr.4, 2023].

[67] *Analog Devices Inc.* ADXL1367: product datasheet and information, [Online]. Available: https://www.analog.com/en/products/adxl367.html. [Accessed Apr.4, 2023].

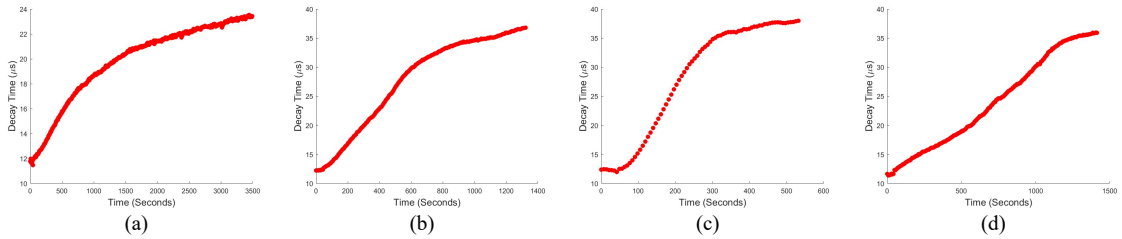

Figure 59: Initial test of (a) abdomen (b) bicep (c) cheek (d) chest.

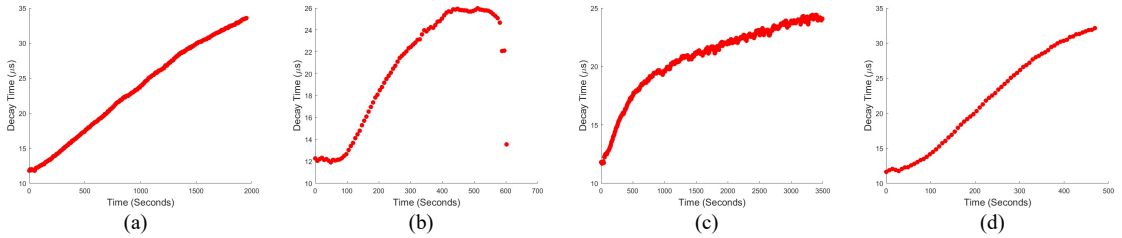

Figure 60: Initial test of (a) clavicle (b) back of ear (c) forearm (d) neck.

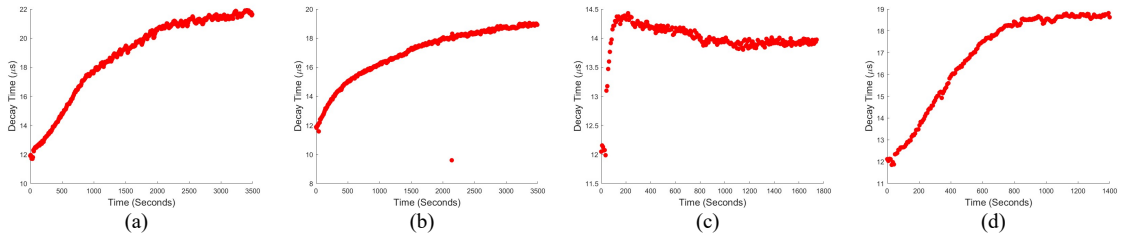

Figure 61: Initial test of (a) shin (b) thigh (c) thumb (d) wrist.